Materials Science & Engineering A 975 (2026) 150925

Contents lists available at ScienceDirect

Materials Science & Engineering A

journal homepage: www.elsevier.com/locate/msea

Fatigue response of 10H2M steel after prolonged service in the giga-cycle regime using ultrasonic fatigue testing

Ved Prakash Dubey [a,b], Marzena Pawlik [b], Dominika Przygucka [c], Pankaj Kumar [a], Stanisław Jóźwiak [c], Zbigniew L. Kowalewski [a], Paul Wood [b], Mateusz Kopec [a,b,*]

[a] Institute of Fundamental Technological Research, Polish Academy of Sciences, Pawinskiego 5B, Warsaw, 02-106, Poland
[b] Institute for Innovation in Sustainable Engineering, College of Science and Engineering, University of Derby, DE22 1GB, UK
[c] Institute of Materials Science and Engineering, Military University of Technology, Kaliskiego 2 Str., Warsaw, 00-908, Poland

ARTICLE INFO

Keywords:
Very high cycle fatigue
Power plant steels
Failure mechanisms
Ultrasonic testing
Fracture mechanisms

ABSTRACT

In this work, the very-high-cycle fatigue (VHCF) response of 10H2M steel in the as-received state and after 280,000 h of service at 540 °C under pressure was analysed. Although after prolonged service, only a moderate decrease in yield strength was observed, fatigue performance was significantly reduced in the stress range applied. Fractographic analysis revealed that in both material states, fatigue cracks initiated near the surface, with carbides acting as preferential nucleation sites. In the as-received material, cracks propagated in a relatively uniform, transgranular manner with ductile overload fracture at final failure. In contrast, the prolonged-service material exhibited rougher fracture surfaces with more frequent crack deflections and secondary cracking, linked to carbide coarsening due to service. The results demonstrate that prolonged exposure does not fundamentally change the surface-dominated initiation mechanism but intensifies the role of carbides and boundary-related defects, thereby reducing fatigue resistance. EBSD-informed finite-element representative volume element (RVE) simulations further revealed that prolonged service exposure increased the local carbide/matrix stress concentration factor, providing micromechanical evidence for the experimentally observed deterioration in fatigue resistance. Additionally, X-ray diffraction (XRD) analysis confirmed thermodynamically driven carbide precipitation and crystallographic evolution, characterised by reduced carbon supersaturation, crystallite refinement, residual micro-stress relaxation and texture evolution following long-term service exposure.

1. Introduction

10H2M steel has been widely used in the power engineering sector for several decades [1]. Its chemical composition, characterised by the presence of chromium and molybdenum, provides a desirable combination of high-temperature strength, good resistance to creep, and structural stability during long-term exposure to elevated service conditions. In addition, the steel is characterised by good weldability and toughness, making it suitable for the manufacture of thick-walled components that operate under both thermal and mechanical stresses. Consequently, 10H2M steel is still widely used for steam pipelines, boiler drums, collectors, and other pressure-bearing components in fossil-fuel power plants. The reliability of these installations, and thus the safety of large-scale energy production, is directly related to the performance and degradation behaviour of this material under prolonged-service conditions [2].

Since many power plants worldwide continue to operate beyond their originally designed service lifetimes, the issue of monitoring and assessing the mechanical integrity of structural steels has gained critical importance [3]. Extended operation at high temperatures accelerates microstructural changes such as the coarsening and spheroidization of carbides, temper embrittlement, and the initiation of creep cavities along grain boundaries [4]. These changes can significantly alter the mechanical response of the steel, particularly its fatigue resistance, which may accelerate the initiation of cracks under cyclic loading. Since fatigue failures often occur without visible macroscopic features, understanding the post-service fatigue performance of steels is extremely important for safe operation and life extension of power plant components. Ultrasonic fatigue testing has emerged as a powerful technique in this context for investigating the very-high-cycle fatigue (VHCF) behaviour of metallic materials [5]. In this method, specially designed specimens are excited at their longitudinal resonant frequency (typically

* Corresponding author. Institute of Fundamental Technological Research, Polish Academy of Sciences, Pawinskiego 5B, 02-106, Warsaw, Poland.
E-mail address: mkopec@ippt.pan.pl (M. Kopec).

https://doi.org/10.1016/j.msea.2026.150925
Received 24 March 2026; Received in revised form 10 August 2026; Accepted 11 August 2026
Available online 11 August 2026

20 kHz) using a piezoelectric transducer, enabling rapid accumulation of loading cycles while maintaining controlled stress amplitudes [6]. Compared with conventional servo-hydraulic testing, ultrasonic fatigue testing significantly reduces the time required to reach giga-cycle lifetimes, making laboratory-based investigation of the VHCF regime both practical and economical. In addition, the technique can be readily combined with in-situ temperature monitoring and post-fatigue microstructural characterisation, providing valuable insights into damage accumulation, crack initiation mechanisms and the influence of long-term service degradation on fatigue behaviour.

Fatigue behaviour in the VHCF regime is governed by a complex interaction between cyclic plastic deformation, microstructural evolution and crack initiation mechanisms, which are strongly dependent on the material and the nature of defects. Recent reviews have highlighted that, unlike conventional fatigue, VHCF failure is often controlled by microstructural heterogeneities, where the characteristics of defects, including their size, morphology, location and associated local stress concentration, play a decisive role in determining the dominant crack initiation mechanism and fatigue life. Consequently, non-metallic inclusions, pores, lack-of-fusion defects and surface imperfections may promote different failure mechanisms depending on the material strength, microstructure and manufacturing route [7–9]. In additively manufactured metallic materials, including Ti6Al4V [10], AlSi10Mg [11], AlSi12 [12], Inconel 718 [13] and 316L stainless steel [14], fatigue performance has been shown to be primarily governed by manufacturing-induced defects, which may promote crack initiation either from the surface or from internal defects depending on their size, morphology and distribution. Similarly, the VHCF response of LPBF-fabricated Nitinol has been reported to be strongly influenced by process-induced porosity, where local stress concentrations around defects control crack nucleation under ultrasonic fatigue loading [15].

In addition to the additive manufactured materials, ultrasonic fatigue testing has been widely adopted for long-term assessment of service life of different structural materials, including S275JR [16,17], S355JR [18], cast steel G42CrMo4 [19], AISI-SAE 52100 [20]. Different microscopic damage evolution mechanisms have also been reported for steels with different strength levels. Krupp et al. [21] reported that tempered martensitic 50CrMo4 steel exhibited surface crack initiation at prior austenite grain boundaries in the medium-strength condition (37 HRC), whereas the high-strength condition (57 HRC) failed by subsurface crack initiation at non-metallic inclusions accompanied by fine granular area (FGA) formation. In a similar study, Pyttel et al. [22] investigated smooth and notched specimens of quenched and tempered 42CrMoS4 steel and nodular cast iron in the VHCF region. The smooth specimens of 42CrMoS4 steel failed predominantly from oxide inclusions, with the higher-strength steel (1350 MPa) exhibiting mainly internal crack initiation, whereas the lower-strength steel (1100 MPa) showed predominantly surface or near-surface crack initiation. In contrast, notched specimens consistently exhibited surface crack initiation due to the dominant effect of notch-induced stress concentration. Whereas, shrinkage cavities controlled crack initiation in nodular cast iron. Pyttel et al. [22] also reported that intrinsic defects can be treated as pre-existing cracks within a fracture mechanics framework, providing a rational basis for assessing the influence of defects on fatigue strength in the VHCF regime. Similarly, Schönbauer et al. [23] investigated the influence of intrinsic and artificial defects on the VHCF behaviour of 17-4 PH precipitation-hardened stainless steel. For smooth specimens, fatigue fracture initiating predominantly from intrinsic non-metallic inclusions was observed even beyond 10^{10} cycles. In contrast, specimens containing artificial defects, including drilled holes, corrosion pits and circumferential notches, did not fail beyond approximately 10^7 cycles. The results revealed that fatigue performance is governed not only by defect size but also by defect geometry and notch root radius, indicating that defects with comparable dimensions may produce significantly different fatigue limits because of differences in local stress concentration.

Although the VHCF behaviour of many metallic materials has been extensively investigated, limited research is available regarding the influence of long-term high-temperature service exposure on the fatigue performance of ferritic-bainitic Cr-Mo steels. In particular, the effects of service-induced microstructural degradation on fatigue life, crack initiation mechanisms and microscopic damage evolution beyond 10^7 cycles have not been systematically established. Therefore, the present study aims to investigate the fatigue response of as-received and service-exposed 10H2M steel in the giga-cycle regime using ultrasonic fatigue testing. X-ray diffraction (XRD) analysis is employed to characterise the phase constitution, crystallite size, residual stress state and texture evolution, while fractographic analysis, electron backscatter diffraction (EBSD) and kernel average misorientation (KAM) analysis are used to correlate the fatigue performance with microstructural degradation induced by prolonged service exposure. Furthermore, EBSD-informed finite-element representative volume element (RVE) simulations are performed to quantify the influence of service-induced microstructural degradation on local stress and strain partitioning. The numerical analysis is further used to examine the size-dependent fatigue crack initiation transition associated with carbide evolution and to establish the relationship between local deformation behaviour and the experimentally observed VHCF performance. The findings are expected to contribute to a more reliable evaluation of structural integrity in aged components and to provide guidance for extending the safe operating life of power plant installations.

2. Materials and methods

2.1. Materials

The wire-cut specimens were extracted from 10H2M steel pipe sections of 1m long delivered in both the as-received state and after prolonged service for 280,000 h at a high temperature of 540 °C under the internal pressure of 2.9 MPa, as specified by the power plant maintenance service. The prolonged service resulted in the notable phase evolution of the 10H2M steel microstructure (Fig. 1). The as-received ferritic-bainitic microstructure exhibited the packets of lath or plate-shaped ferrite (Fig. 1a). Long-term service at a temperature of 540 °C, as indicated by the CCT diagram [24], led to the precipitation of carbides from the primary bainitic microstructure. This process reduced the degree of supersaturation of the bainite and promoted the formation of a

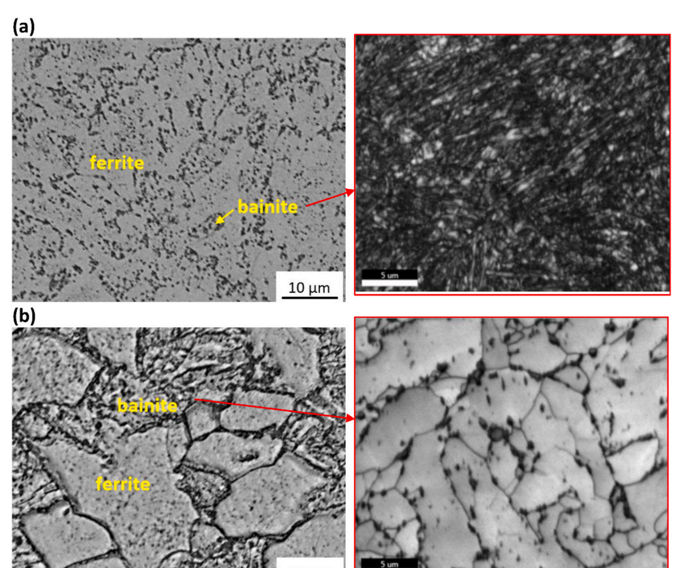

Fig. 1. Microstructure of 10H2M steel in the as-received state (a) and after 280,000 h of service (b), with enlarged views of the bainite regions.

higher volume fraction of carbide precipitates, particularly along the boundaries of the original martensitic microstructure (Fig. 1b). Consequently, the microstructural evolution reflects thermally activated diffusion processes that contribute to the redistribution of carbon and the stabilisation of secondary phases [1,25].

2.2. Mechanical testing

Hourglass-shaped, double-threaded specimens used for either standard tensile or fatigue tests were wire-cut and machined from the as-received and prolonged-service pipelines made of 10H2M steel. The specimen geometry is shown in Fig. 2a. Uniaxial tensile tests were executed to determine material characteristics and typical strength parameters, including Young's modulus and yield strength at a strain rate equal to 2×10^{-4} s^{-1}. These material parameters were subsequently used as input for ultrasonic specimen design and for defining the stress amplitude range applied during fatigue testing. Ultrasonic fatigue testing was performed on a Shimadzu USF2000 system (Fig. 2) operating at a nominal frequency of 20 kHz and standardised by the Japan Welding Engineering Society [26]. Unlike conventional fatigue testing, ultrasonic fatigue requires the specimen to resonate in the longitudinal vibration mode at the operating frequency [15]. Therefore, the specimen geometry was designed according to the resonance requirements of the ultrasonic testing system rather than conventional ASTM fatigue specimen dimensions. Specimen geometry was determined by Shimadzu software based on the input material properties (Young's modulus and density) to resonate at 20 kHz. Based on this input, the software calculated the specimen length, gauge diameter, transition radii and shoulder geometry. The designed geometry was accepted only when the calculated resonant frequency was within the operating range of the testing system (19.5-20.5 kHz). A sinusoidal waveform at stress ratio $R = -1$ was employed for fatigue loading. The specimen was mounted at the top (horn) and bottom in accordance with the manufacturer's recommendations. Cyclic stresses were generated through horn displacement and correlated with the maximum stress within the reduced gauge section. The range of stress amplitude from ±275 MPa to ±400 MPa was tested. Prior to each test, the specimens were verified by a frequency check test to ensure resonance at 20 kHz.

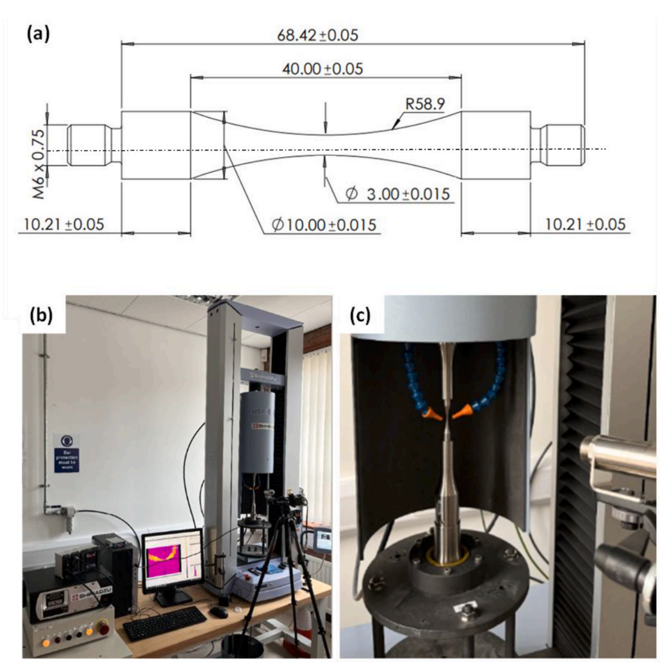

Fig. 2. Engineering drawing of the double-threaded hourglass specimen (a); general view of the experimental setup (b) and close-up view of the specimen (c).

Because the heating is a significant challenge for structural steels in ultrasonic fatigue testing [5], it is crucial to ensure that the temperature is properly controlled. The testing setup was equipped with an internal cooling system composed of air-cooling nozzles that were pointed at the sample to suppress intensive heating. In addition, intermittent (pulse-pause) loading was employed, where specimens were excited for a brief period of time, followed by a cooling period. Specimen temperature was monitored through the Optris Xi80 LT ETH smart thermal camera, combining pyrometer functions with thermal imaging capabilities. Thermal data, including spatial distribution, were recorded using PIX Connect software with the average temperature measured at the centre of the gauge section. Thermal imaging was used primarily to monitor relative temperature evolution and to ensure stable thermal conditions during ultrasonic fatigue testing rather than to obtain absolute temperature measurements. Since all specimens were manufactured from the same material and exhibited comparable surface finish, emissivity was assumed constant throughout the comparative analysis and temperature control criteria. The temperature data was recorded with a frequency of 20 Hz for all tests. All samples were loaded for a 110-ms oscillation time, while the cooling pause varied from 2 to 5 s, depending on the amplitude. The temperature of the specimens was kept below 30 °C throughout the test using a combination of a cooling nozzle and intermittent driving [17]. The test was automatically terminated by the built-in crack detection failure when the frequency of the specimen fell outside the 19.5 – 20.5 kHz frequency range. Specimens surviving up to 10^9 cycles were considered runouts.

2.3. Microstructural observations

The microstructural observations and fracture surface examinations were performed using a JEOL JSM-6360LA scanning electron microscope operated at an accelerating voltage of 20 kV in the secondary electron (SE) imaging mode. The microstructural characterisation was complemented by electron backscatter diffraction (EBSD) analysis carried out using an FEI Quanta 3D FEG scanning electron microscope equipped with EDAX EBSD and EDS detectors and operated at an accelerating voltage of 20 kV. The specimens were examined at a specimen tilt angle of 70°, using a working distance of 19 mm and an EBSD step size of 1 μm. The acquired EBSD data were indexed using TEAM EBSD Analysis System. Post data analysis, comprising phase segmentation, grain reconstruction, kernel average misorientation (KAM) and geometrically necessary dislocation (GND) density calculations were extensively performed using the MTEX toolbox via MATLAB software. Low-angle grain boundaries (LABs) were defined as boundaries with misorientation angles between 2° and 15°, while high-angle grain boundaries (HABs) were defined as those exceeding 15°. KAM maps were calculated using the first-neighbour approach with a maximum misorientation threshold of 5° to evaluate local plastic deformation. GND density was subsequently estimated from the KAM data using the standard Pantleon relationship $\rho_{GND} = \left(\frac{2\theta_{KAM}}{u \cdot b}\right)$ [27]. In this equation, θ_{KAM} is the average misorientation (in radians), u is the EBSD step size, and b is the magnitude of the Burgers vector of the ferritic α-Fe matrix ($b = 0.248\ nm$). Prior to microscopy, the specimens were hot-mounted and mechanically prepared by successive grinding and polishing, including planar polishing on a Struers MD-Largo platen with a 2 μm diamond suspension, followed by final polishing on a Metprep® MD-Chem cloth using a 0.04 μm colloidal silica suspension. Optical micrographs were obtained using a Nikon MA220 optical microscope. X-ray diffraction (XRD) measurements were performed to characterise the phase constitution, crystallite size, residual stress state and texture coefficient of the investigated materials. The measurements were carried out using a Rigaku (Tokyo, Japan) Ultima IV diffractometer equipped with Co-Kα radiation (λ = 1.78897 Å), operating at 40 kV and 40 mA. Diffraction patterns were acquired over a 2θ range of 20°-130° using a step size of 0.02° and a scanning speed of 1° min^{-1}.

3. Results

3.1. Mechanical response

The tensile curves in Fig. 3a and the mechanical parameters summarised in Table 1 present the influence of prolonged service on the static strength of 10H2M steel. In the as-received condition, the steel exhibited a yield strength (S_y) of approximately 334 MPa and an ultimate tensile strength (S_u) of 545 MPa, combined with high ductility (elongation ~35%). After 280,000 h of operation at 540 °C, the yield strength reduced by about 26% to 248 MPa, while the ultimate tensile strength remained almost unchanged (543 MPa). The ductility showed a modest increase to 38%, suggesting that microstructural degradation during service primarily reduced the resistance to plastic yielding, without strongly affecting the capacity for uniform plastic deformation. The Young's modulus also showed a slight decrease (from 216 to 208 GPa), consistent with coarsening of the ferritic-bainitic microstructure. The fatigue behaviour, shown in Fig. 3b, revealed a more pronounced effect of service exposure. For the as-received material, fatigue life extended into the very-high-cycle regime, with specimens enduring stresses as high as 365–375 MPa for millions of cycles, and at lower stresses (≤300 MPa) exceeding 10^9 cycles without failure, reaching the run-out threshold. In contrast, the prolonged-service material displayed a substantial reduction in fatigue life across the entire stress range. At 375 MPa, failure occurred in fewer than 3000 cycles, compared to nearly 1.18×10^6 cycles for the as-received condition. Even at intermediate stress amplitudes (e.g., 325 MPa), the fatigue life of the material after prolonged service was reduced by more than an order of magnitude. Although both conditions reached the giga-cycle domain, the prolonged-service specimens consistently failed at lower cycle counts, confirming the strong effect of microstructural degradation on cyclic durability.

3.2. Temperature evolution during ultrasonic fatigue

Fig. 4 presents a typical temperature versus time graph for a specimen under ultrasonic loading. During the pulse, sudden temperature increases were observed. The magnitude of temperature increase depended on the amplitude, as shown in Fig. 5. For example, for a 350 MPa amplitude, the temperature increased by approximately 4° during the pulse. The selected testing conditions, i.e. pulse 110 ms, 5 s cooling pause, and air-cooling nozzles, were sufficient to keep the temperature below 30 °C initially. However, the heat generation would increase as the test progressed. At around 2000 s, corresponding to 8×10^6 cycles, an exponential increase in temperature was observed (Fig. 4). At fatigue failure (9.7×10^6 cycles), the temperature of the specimen reached 85.4 °C. The peak temperature ranged from 34.5 to 275 °C depending on the amplitude. However, the correlation between peak temperature and stress amplitude could be affected by the thermal camera sampling rate (50 ms). The local increase in temperature is likely associated with the propagation of a fatigue crack in the specimen, as observed by Mayer [6].

Table 1
Mechanical properties of 10H2M steel before and after service.

Material state	S_u [MPa]	S_y [MPa]	A[%]	E [GPa]	ν
As-received	545(±5)	334(±4)	35%(±1)	216	0.33
Prolonged service	543(±5)	248(±3)	38%(±1)	208	0.33

Table 2 presents a summary of the temperature at failure recorded by the thermal camera for as-received and after prolonged service specimens at three amplitude levels. In general, it was observed that as-received specimens experienced higher dissipation spikes right at the failure compared to specimens after prolonged use. This could be related to change in local plasticity and cracking caused by structural changes caused by operating conditions [6]. The precipitation of carbides from the primary bainitic microstructure led to a reduction of internal stresses within the subsequently formed martensitic regions. As a consequence, the material exhibited facilitated internal friction during cyclic loading, which promoted the initiation and accumulation of microstructural defects. This process ultimately resulted in a deterioration of fatigue strength. The lower temperatures recorded for the prolonged-service specimens should not be interpreted as evidence of increased energy dissipation (Fig. 5b). Instead, they indicate that a smaller fraction of the mechanical work was converted into heat through distributed cyclic plastic deformation. In metallic materials subjected to ultrasonic fatigue, heat generation primarily originates from irreversible dislocation motion, internal friction and local microplasticity [28,29]. The as-received material, characterised by a finer and more homogeneous ferritic-bainitic microstructure, was able to accommodate cyclic deformation over a larger material volume, resulting in greater heat generation prior to failure. In contrast, prolonged service promoted carbide coarsening and redistribution, leading to pronounced local stress concentrations and highly localised deformation. Consequently, fatigue damage accumulated more rapidly near carbide-rich regions and degraded boundaries, reducing the extent of distributed plastic deformation and therefore the measured surface temperature before failure.

It should be noted that the ultrasonic fatigue tests were performed under displacement-controlled resonance conditions. During crack propagation, localised changes in the specimen stiffness occur, resulting in an increase in the local strain amplitude despite the externally imposed displacement remaining nearly constant. Consequently, the infrared camera records the surface temperature associated with

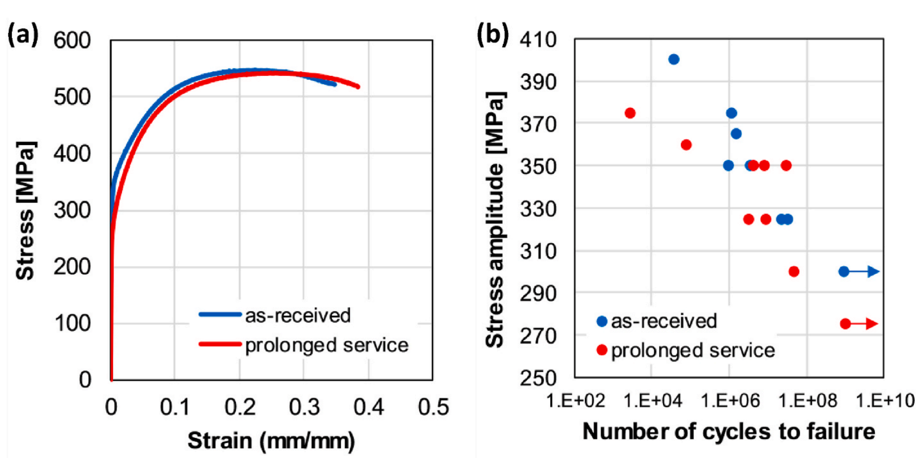

Fig. 3. Representative tensile curves (a) and S-N curves (b) of 10H2M steel in the as-received state and after prolonged service.

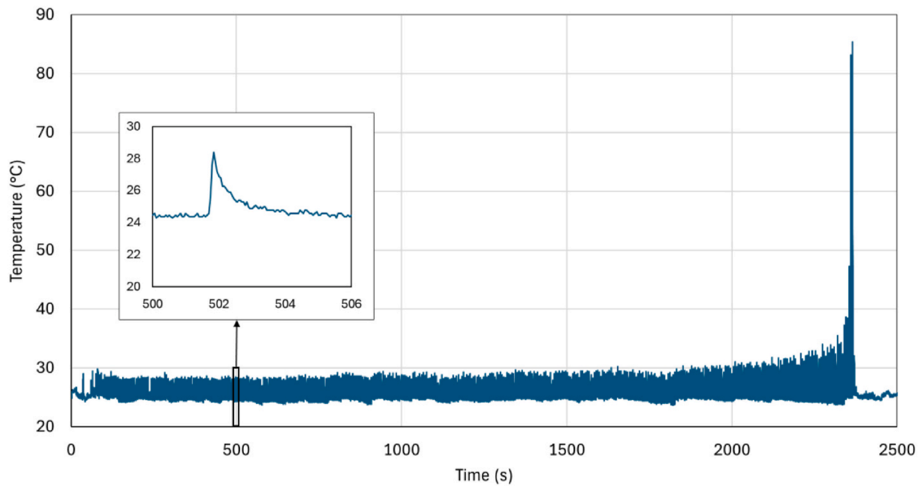

Fig. 4. Temperature history of the as-received specimen during ultrasonic fatigue testing at a stress amplitude of 350 MPa.

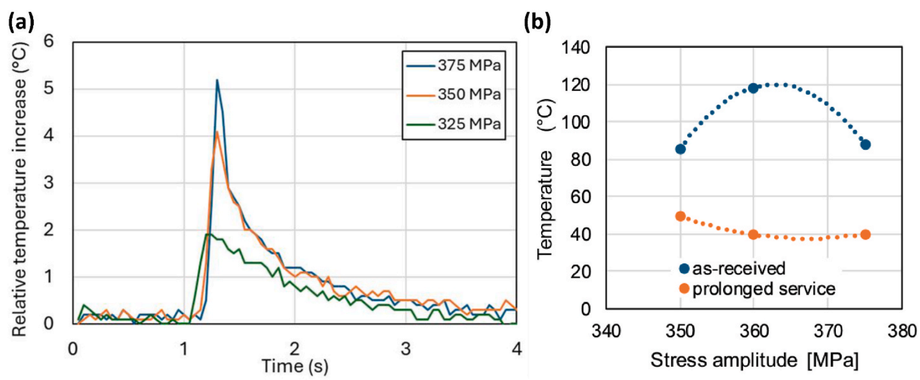

Fig. 5. Relative temperature increases during the intermittent driving for the as-received specimens at three different amplitudes (a); temperature change on the surface of the samples as a function of the stress amplitude (b).

Table 2
Temperature recorded at fatigue failure for the as-received and prolonged-service specimens at different stress amplitude.

Stress amplitude [MPa]	Temperature at failure [°C]	
	As-received	Prolonged service
375	87.9	40.0
360	118.3	39.6
350	85.4	49.4

localised plastic deformation and crack propagation rather than the absolute temperature arising solely from homogeneous cyclic loading. Therefore, the temperatures reported at failure should be interpreted as comparative indicators of energy dissipation and damage evolution between the investigated material conditions rather than absolute thermodynamic quantities. Nevertheless, because identical testing conditions, specimen geometry, loading frequency and air-cooling strategy were employed throughout the study, the observed temperature differences between the as-received and prolonged-service materials provide a reliable basis for comparing their relative fatigue behaviour.

3.3. Fractographic analysis of 10H2M steel subjected to USF

Detailed SEM observations of the fracture surfaces revealed differences in crack initiation and propagation between the as-received and after prolonged service 10H2M steel specimens, despite both showing surface-related origins (Fig. 6). In the as-received material, fatigue cracks nucleated at or near the specimen surface. Initiation sites were probably associated with machining traces, shallow notches, or slip steps intersecting fine carbides [30].

One should note that for both stress amplitudes, the area of exact crack initiation was hard to identify. However, each fracture zone could be clearly distinguished; thus, the area of potential fracture was investigated. On the other hand, the surrounding initiation zones exhibited smooth facets with clear transgranular morphology, indicating localised plastic slip as the dominant nucleation mechanism. The propagation zone was relatively uniform and planar, reflecting the homogeneous microstructure of the steel before service.

On the other hand, the fracture morphology of the prolonged-service steel was more complex. Prolonged high-temperature exposure led to the coarsening and redistribution of carbides, particularly along grain and subgrain boundaries. These carbides acted as preferential stress concentrators, serving as dominant initiation sites near the specimen surface [31]. In most cases, the crack origin could be traced directly to a coarse carbide particle or carbide cluster fractured or decohered from the surrounding matrix [32]. Unlike the as-received specimens, initiation zones in the prolonged-service material appeared more irregular, with multiple microcracks often near the main crack origin. Stable crack growth in the prolonged-service specimens was, however, more uniform, and the propagation surfaces appeared rougher, with frequent deflections of the crack front caused by microstructural heterogeneity. SEM images revealed mixed transgranular and quasi-cleavage features, suggesting local embrittlement around carbides and degraded boundaries. The presence of elongated dimples around carbides indicates that

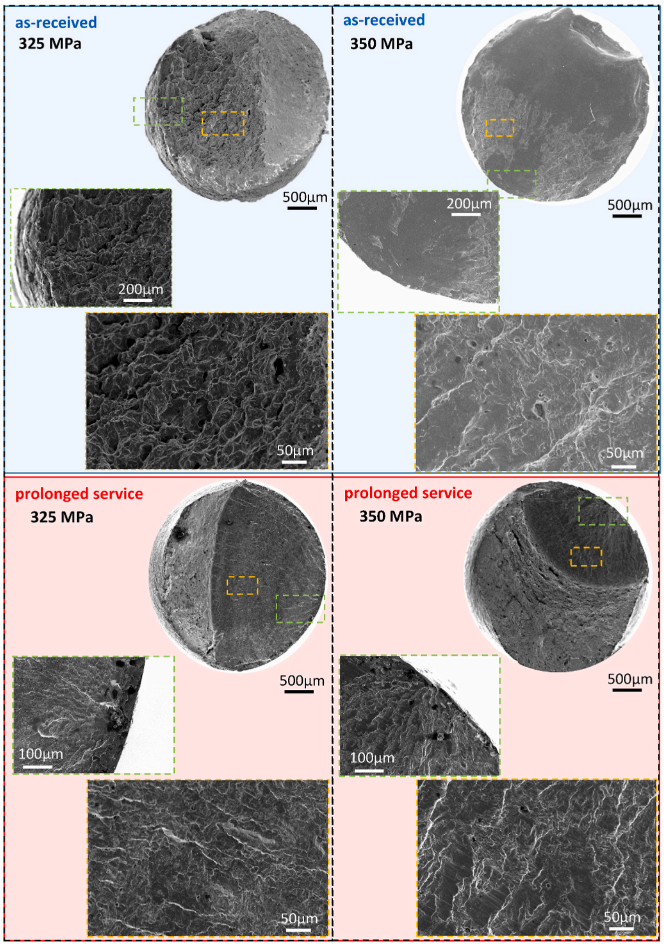

Fig. 6. Fractographic observations of 10H2M steel after ultrasonic fatigue testing at stress amplitudes equal to 325 MPa and 350 MPa, respectively.

carbide/matrix interfaces served as preferential void nucleation sites during cyclic loading. The overload zones also displayed distinct differences between the two material states. In the prolonged-service condition, the final rupture was dominated by ductile dimples of uniform size and shape, consistent with high local plasticity. In contrast, the as-received steel exhibited a mixed fracture mode, where ductile dimples coexisted with quasi-cleavage facets and locally brittle areas. These features suggest that while ductile rupture remained the dominant failure mechanism, the service-induced microstructural changes, particularly carbide coarsening and segregation, reduced the local ductility and promoted premature brittle cracking. The present fractographic observations are limited to specimens fractured at stress amplitudes equal to 325 and 350 MPa, respectively. For the as-received material, specimens tested at 300 MPa reached the run-out criterion of 10^9 cycles without failure, while for the prolonged-service material the run-out criterion was reached at 275 MPa. Consequently, fracture surfaces at these lower stress amplitudes were not available for examination.

3.4. EBSD characterisation

EBSD was employed to evaluate the crystallographic orientation, grain boundary character, and local strain distribution in 10H2M steel subjected to USFT. The inverse pole figure (IPF) maps presented in Fig. 7 illustrate the crystallographic orientation of grains for both the as-received material and the steel after prolonged service. In both conditions, the microstructure consists of fine lath packets typical of tempered martensitic/bainitic steels. The application of cyclically varying stress, irrespective of the initial material condition or the level of stress amplitude, leads to the development of a distinct crystallographic texture. This texture consistently forms along the same crystallographic planes, predominantly oriented in the <100> direction. This observation suggests that the cyclic loading promotes a preferential reorientation of grains or activation of specific slip systems, resulting in the emergence of a well-defined texture even in materials that were initially texture-free. However, noticeable differences can be observed in the degree of microstructural fragmentation. The as-received steel exhibits more uniform orientation regions corresponding to relatively intact martensitic laths and subgrain packets. In contrast, the material after prolonged service shows a higher level of orientation fragmentation and irregular grain morphology. This feature suggests partial recovery and subgrain rearrangement caused by long-term exposure to elevated temperature. Such processes are commonly associated with dislocation annihilation, carbide coarsening, and local redistribution of strain fields during service [33].

Additional information about the local strain distribution is provided by the kernel average misorientation (KAM) maps shown in Fig. 8. The KAM parameter reflects the local lattice curvature and therefore correlates with geometrically necessary dislocation density. In the as-received steel, the KAM maps reveal relatively low misorientation values within the grain interiors, indicating a fairly homogeneous dislocation distribution. Elevated KAM values are primarily concentrated near grain boundaries and around carbide particles, suggesting local strain accumulation in these regions.

In contrast, the prolonged-service steel exhibits noticeably higher KAM values and a more heterogeneous misorientation distribution. Regions of increased local misorientation are frequently observed near grain boundaries and along areas enriched with carbide precipitates. This indicates that prolonged service leads to localised lattice distortion and strain accumulation. Such behaviour can be attributed to microstructural degradation mechanisms including carbide coarsening, recovery of the martensitic substructure, and redistribution of dislocations during long-term exposure at elevated temperature.

To thoroughly substantiate the impact of service-induced microstructural degradation, a quantitative correlation was established between the localised micromechanical strain and the macroscopic fatigue resistance. To ensure statistical reliability, the fatigue life values utilised for this correlation specifically at the 350 MPa stress amplitude represent the logarithmic average of three independent, repeated tests for each material condition. By mapping the mean KAM and GND density values directly against these statistically averaged fatigue lives, a distinct inverse relationship was identified across the evaluated stress regimes as shown in Fig. 9.

As evidenced from Fig. 9, at an applied stress amplitude of 300 MPa, the as-received 10H2M steel exhibited negligible strain localisation (mean KAM of $\sim 1.3^{\circ}$), correlating with an extended fatigue life reaching the giga-cycle run-out threshold (1×10^9 cycles). Conversely, at the identical stress amplitude, the prolonged-service material exhibited severely elevated intragranular misorientation (mean KAM of $\sim 2.0^{\circ}$), correlating quantitatively with premature failure at approximately 5×10^7 cycles.

The physical driver of this localised strain accumulation can be elucidated through the material's macroscopic cyclic deformation response as depicted in Fig. 10. Because direct measurement of stabilised cyclic hysteresis loops is physically constrained under 20 kHz ultrasonic fatigue testing, we mathematically modelled the macroscopic cyclic deformation response to provide a physical explanation for this correlation. The cyclic stress-strain behaviour was governed by the Ramberg-Osgood relationship [34]:

$$\frac{\Delta\varepsilon}{2} = \frac{\Delta\sigma}{2E} + \left(\frac{\Delta\sigma}{2K'}\right)^{1/n'} \tag{1}$$

The cyclic parameters were predicted from the monotonic tensile results using the robust monotonic-to-cyclic approximation framework

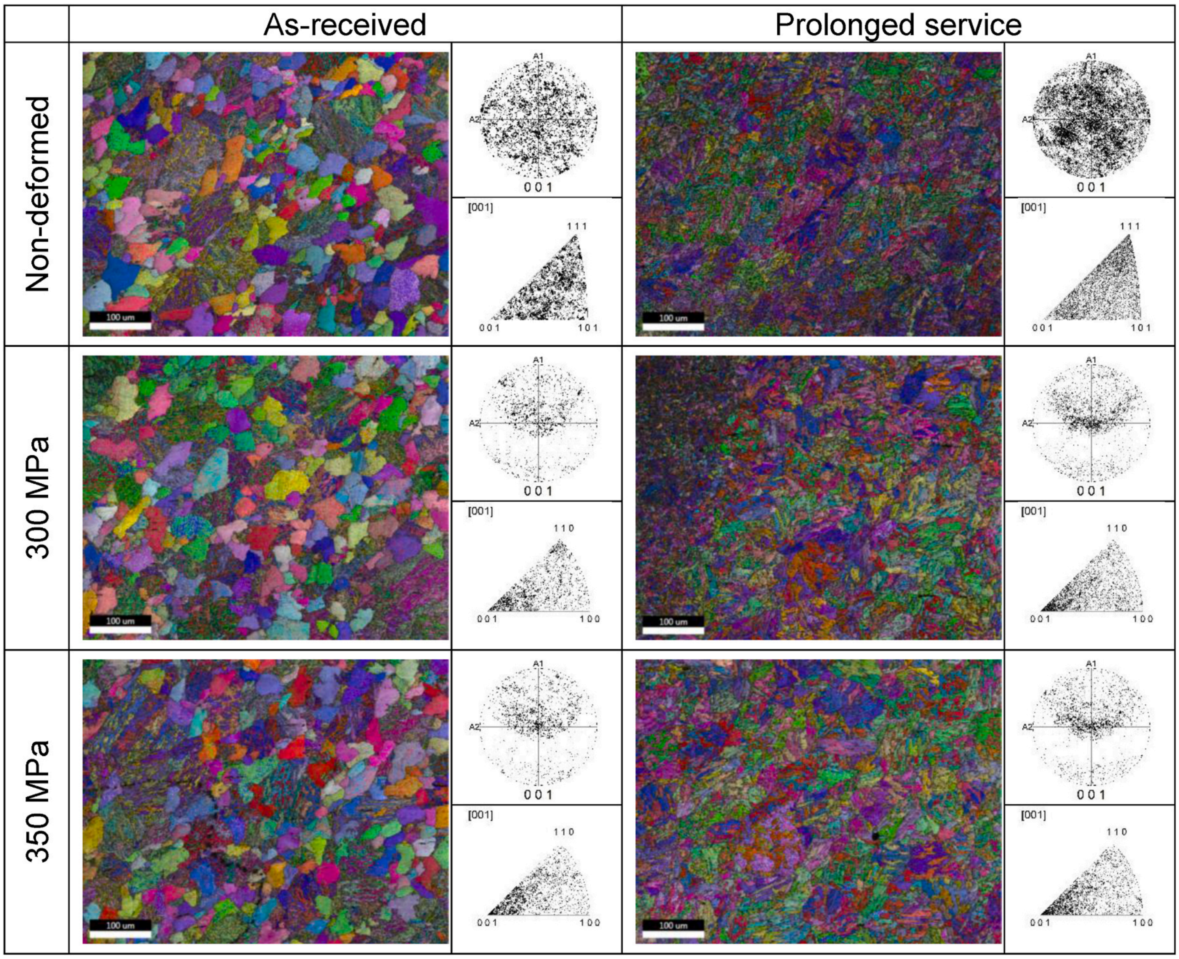

Fig. 7. IPF maps of 10H2M steel in the non-deformed state and after ultrasonic fatigue testing at stress amplitudes of 300 and 350 MPa for the as-received and prolonged-service conditions.

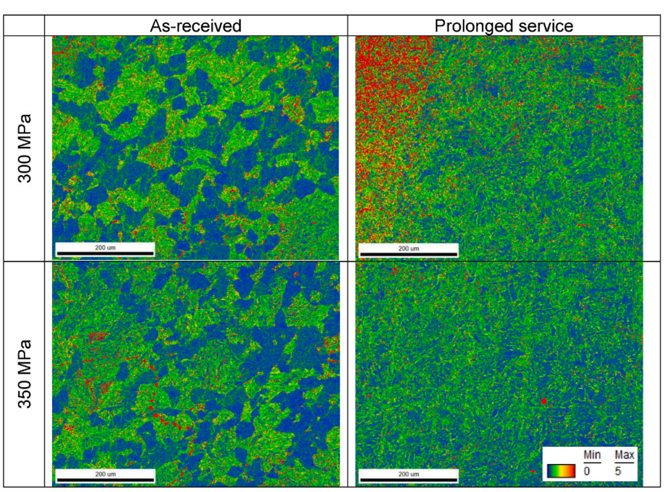

Fig. 8. KAM maps of 10H2M steel after ultrasonic fatigue testing at stress amplitudes of 300 and 350 MPa, respectively.

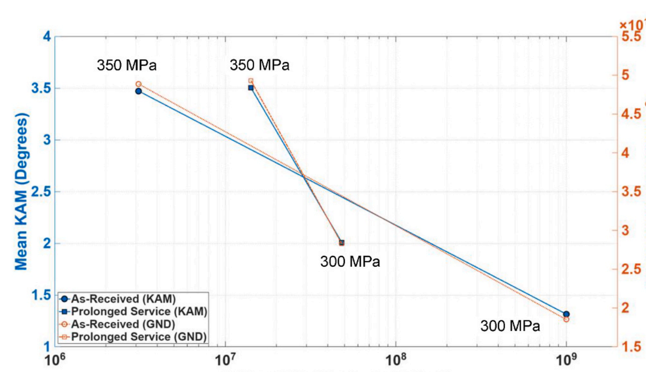

Fig. 9. Quantitative correlation between microstructural strain localisation (measured via mean KAM and GND density) and the statistically averaged fatigue life for the as-received and prolonged-service 10H2M steel across the evaluated stress amplitudes.

established by Lopez and Fatemi [35] for steels. Because both material states exhibited an ultimate-to-yield strength ratio $(S_u/S_y) > 1.2$, the cyclic yield strength $\left(S_y'\right)$, cyclic strength coefficient (K'), and cyclic strain hardening exponent (n') were calculated using their explicit governing equations:

$$S_y' = 0.75 \cdot (S_y) + 82 \tag{2}$$

$$K' = 1.16 \cdot (S_u) + 593 \tag{3}$$

$$n' = -0.33 \cdot \left(\frac{S_u}{S_y}\right) + 0.40 \tag{4}$$

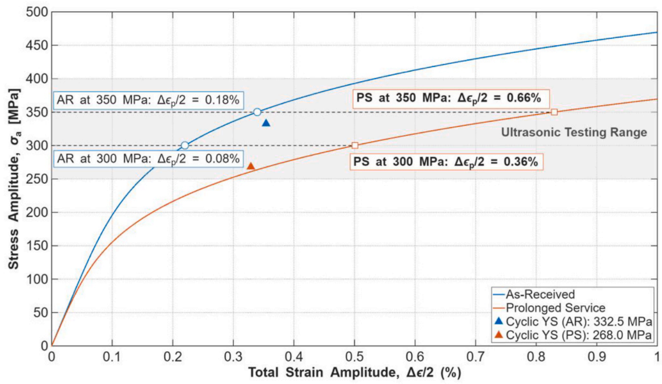

Fig. 10. Predicted cyclic stress-strain response for the as-received (AR) and prolonged-service (PS) 10H2M steel demonstrating the service-induced reduction in cyclic yield strength and the corresponding severe elevation in cyclic plastic strain amplitude accommodated by the degraded microstructure at equivalent stress levels.

The corresponding macroscopic cyclic stress-strain curves (Fig. 10) were analytically generated by plotting the Ramberg-Osgood relationship parameterised with the K' and n' values derived from the aforementioned monotonic-to-cyclic approximations. Utilising these explicit governing equations ((2) - (4)), the service-induced microstructural degradation substantially lowered the macroscopic cyclic yield strength from 332.5 MPa (as-received) to 268 MPa. As demonstrated in Fig. 10, at a given stress amplitude of 300 MPa, the model dictates that the prolonged-service material is forced into a highly plastic regime accommodating a cyclic plastic strain amplitude $\left(\Delta\varepsilon_p/2\right)$ of 0.36% which is 4.5 times higher than the plastic strain amplitude accommodated by the as-received material $\left(\frac{\Delta\varepsilon_p}{2}=0.08\right)$ under the identical load. A similarly severe disparity is observed at the 350 MPa stress amplitude where the prolonged-service material accumulates a cyclic plastic strain amplitude of 0.66%, representing a 3.7 times increase compared to the as-received baseline $\left(\frac{\Delta\varepsilon_p}{2}=0.18\right)$.

Conclusively, this continuum-level cyclic plasticity mathematically mirrors the localised strain accumulation captured by the EBSD analysis. The degraded microstructure possesses a diminished capacity to uniformly accommodate cyclic deformation, forcing intense strain localisation at microstructural heterogeneities. The resulting elevation in localised micro-plasticity quantitatively captured by the KAM and GND density metrics, serves as the primary mechanism accelerating fatigue crack nucleation, thereby directly dictating the observed reduction in the statistically verified fatigue life.

The effect of carbide evolution becomes particularly evident when the EBSD results are considered together with the carbide distribution presented in Fig. 11. In the as-received condition, carbides are relatively fine and more uniformly distributed within the matrix and along grain boundaries. Quantitative phase analysis revealed a homogeneous carbide area fraction of approximately 7.9% in the non-deformed as-received condition. Their small size and homogeneous dispersion contribute to a more uniform stress distribution, effectively limiting the formation of pronounced local stress concentrations. As a result, plastic deformation tends to be more homogeneous at the microscale, and no dominant deformation paths are strongly favoured. After prolonged service, however, the carbide population undergoes significant microstructural changes. The carbide area fraction increased to approximately 17.9%, accompanied by pronounced coarsening and localised accumulation of carbides along grain boundaries, packet boundaries and lath interfaces. This coarsening process is typically driven by diffusion-controlled mechanisms such as Ostwald ripening, leading to a reduction in particle number density accompanied by a substantial increase in their average size. Similar mechanisms were reported for creep-resistant steel X20CrMoV12.1 exposed to prolonged high-temperature service [36]. As demonstrated by Yang et al. [37], prolonged thermal exposure in a low-alloy ferritic steel (2.25Cr-1Mo) promotes the dissolution of finer intragranular carbides and the preferential growth and agglomeration of coarse carbides along grain boundaries due to the enhanced diffusion of carbide-forming elements. Consequently, the spatial distribution of strengthening particles becomes increasingly heterogeneous.

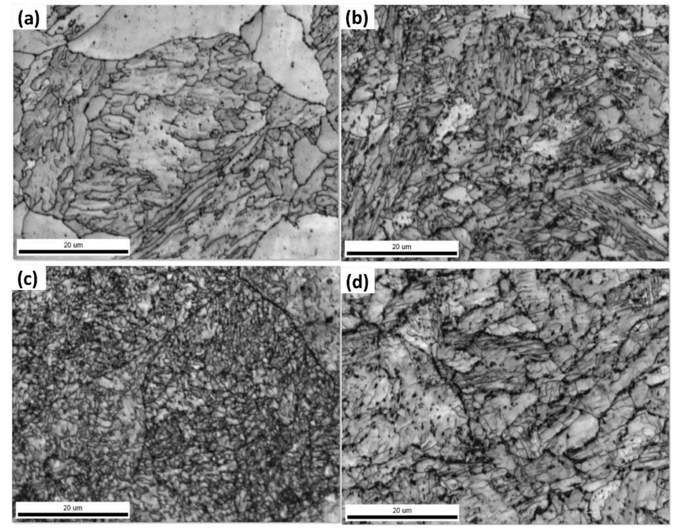

Fig. 11. Carbide distribution in 10H2M steel after USFT at stress amplitude of 300 MPa (a, b) and 350 MPa (c, d) in as-received (a, c) and prolonged-service (b, d) conditions.

3.5. XRD characterisation

X-ray diffraction (XRD) measurements were performed to characterise the phase constitution, lattice parameter, crystallite size, residual stress state and crystallographic texture of the investigated 10H2M steel before and after prolonged service exposure. The corresponding diffraction patterns are presented in Fig. 12, while the lattice parameter, crystallite size, residual stress and texture analyses are summarised in Figs. 13–15. The diffraction patterns shown in Fig. 12 reveal that the as-received 10H2M steel is predominantly composed of a ferritic matrix, accompanied by low-intensity diffraction peaks corresponding primarily to cementite (Fe_3C). After prolonged service, noticeable changes in the relative diffraction peak intensities were observed together with an increased contribution of carbide-related reflections, indicating significant microstructural evolution during long-term exposure at elevated temperature. This phenomenon is commonly referred to as Ostwald ripening [38,39] and involves the precipitation and coarsening of carbides from the supersaturated bainitic ferrite, preferentially along grain boundaries, accompanied by the thermodynamically driven carbide sequence $M_3C \rightarrow M_7C_3 \rightarrow M_{23}C_6$ [40].

No additional crystalline phases were detected after prolonged service, indicating that the observed microstructural evolution is primarily associated with carbide precipitation and redistribution rather than transformation of the ferritic matrix. Further evidence supporting this precipitation mechanism was obtained from the analysis of the lattice parameter of the supersaturated bainitic ferrite, determined using the Nelson–Riley extrapolation function (NRF) (Eq. (5)), as presented in Fig. 13 [41]:

$$NRF = 0.5 * \left(\frac{\cos^2\theta}{\sin\theta} + \frac{\cos^2\theta}{\theta}\right) \quad (5)$$

The determination of the lattice parameter of the supersaturated bainitic ferrite in both the as-received and prolonged-service conditions enabled the carbon concentration within this phase to be quantified

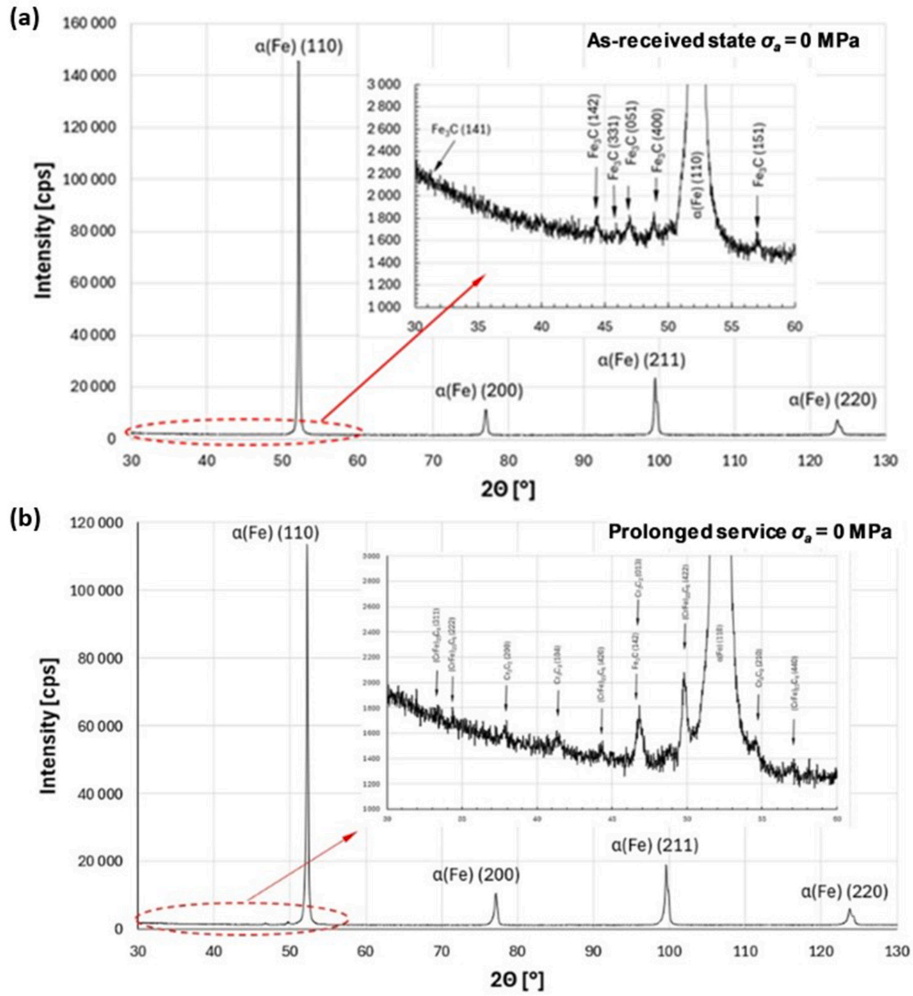

Fig. 12. XRD patterns of 10H2M steel in the as-received condition (a) and after prolonged service exposure (b).

using the empirical relationship proposed in Ref. [42]:

$$a_\alpha = a_{Fe} + 0.039 * x_C + 0.0006 * x_{Mn} - 0.00185 x_{Si} \tag{6}$$

By rearranging Eq. (6) and assuming $a_{Fe} = 2.8664$ Å, together with the nominal chemical composition of 0.5 wt% Mn and 0.3 wt% Si, the carbon content in the supersaturated ferrite was estimated to be approximately 0.22 wt% in the as-received condition. After the precipitation processes induced by prolonged service exposure, the carbon concentration decreased to approximately 0.08 wt%, which is in agreement with previously reported data [43,44]. This pronounced reduction in the carbon supersaturation of the bainitic ferrite confirms the progressive decomposition of lower bainite through carbide precipitation during long-term thermal exposure.

The depletion of carbon from the ferritic matrix promotes the precipitation of cementite from lower bainite, followed by its gradual transformation into coarse $Cr_{23}C_6$ carbides preferentially located along ferrite grain boundaries (Fig. 12b). This evolution is further corroborated by the XRD patterns (Fig. 12b), where the increasing intensity of carbide reflections reflects the progressive precipitation and growth of chromium-rich carbides. These microstructural transformations are accompanied by significant changes in both the crystallite size and the magnitude of Type II residual (micro-) stresses within the ferritic matrix, as illustrated in Fig. 14.

To quantify these parameters, the methodology proposed by Oleszak and Olszyna [45] was adopted. In this approach, the crystallite size (D) and lattice microstrain (ε) are determined from the broadening (β) of X-ray diffraction peaks recorded at different Bragg angles (θ). The analysis considers several assumptions regarding the functional description of diffraction-peak profiles. When both crystallite-size broadening and strain-induced broadening are represented by Cauchy (Lorentzian) functions, the analysis reduces to the classical Williamson–Hall approach, expressed by Eq. (7). Alternatively, assuming Gaussian peak profiles for both contributions leads to the Gauss/Gauss model (Eq. (8)), whereas the Cauchy/Gauss model (Eq. (9)) assumes a Lorentzian contribution associated with finite crystallite size and a Gaussian contribution arising from lattice strain.

$$\beta * \cos\theta = \frac{\lambda}{D} + 4e * \sin\theta \tag{7}$$

$$\beta^2 * \cos^2\theta = \left(\frac{\lambda}{D}\right)^2 + 16e^2 * \sin^2\theta \tag{8}$$

$$\beta^2 * tg^2\theta = \frac{\lambda}{D} * \left(\frac{\beta}{tg\theta * \sin\theta}\right) + 16e^2 \tag{9}$$

The quality of each linear approximation was evaluated using the coefficient of determination (R^2), corresponding to the square of the Pearson correlation coefficient. For all three analytical approaches, R^2 exceeded 0.90, indicating excellent agreement between the experimental data and the adopted line-profile models. Consequently, reliable average values of the ferritic crystallite size (Fig. 14d) and the Type II residual stress (Fig. 14e) were determined for both investigated material conditions. The observed evolution of crystallite size and residual microstress correlates closely with the precipitation processes and the

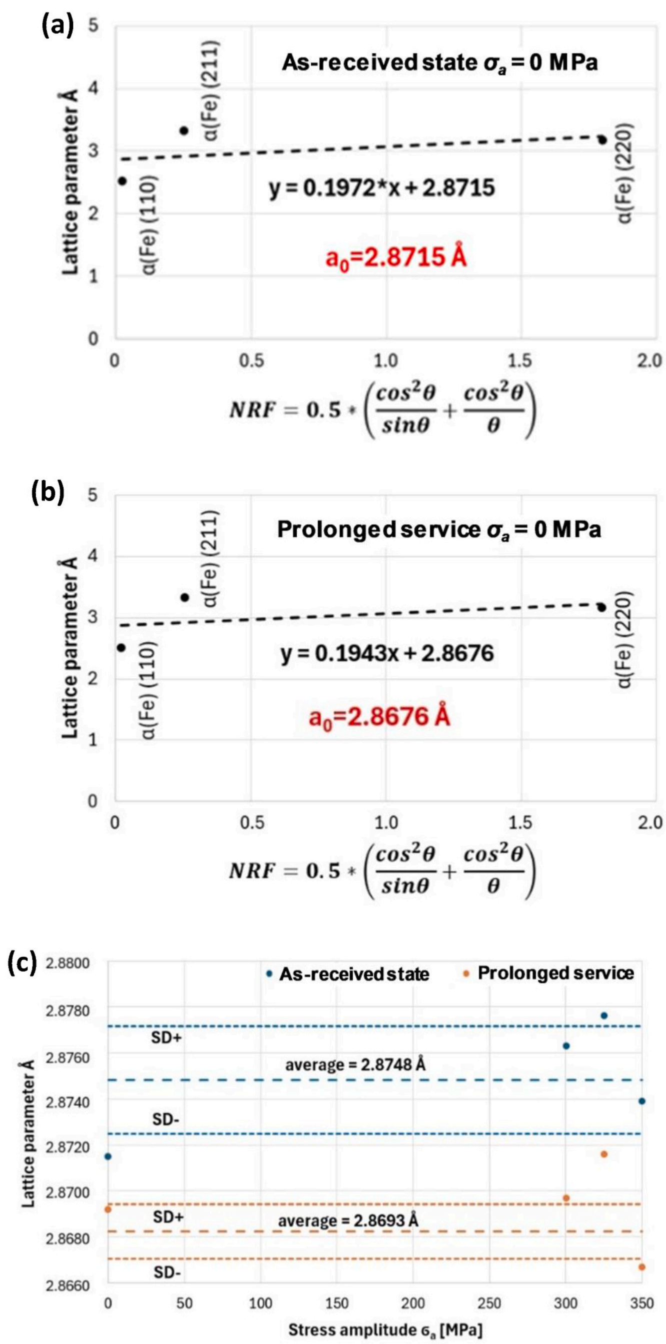

Fig. 13. Determination of the lattice parameter of the ferritic matrix using the Nelson–Riley extrapolation method for non-deformed specimens in the as-received condition (a) and after prolonged service exposure (b). The averaged lattice parameter values of ferrite for both conditions (c).

thermal history summarised in Table 2. In the as-received condition, 10H2M steel exhibits a lower bainitic microstructure in which the ferritic matrix remains highly supersaturated with carbon and contains a dense distribution of fine cementite precipitates. This microstructure generates considerable lattice distortions, thereby increasing internal microstresses and impeding both the nucleation and motion of crystalline defects. As a result, the size of the coherent diffraction domains (crystallites) remains relatively large. Following prolonged service exposure, however, the progressive coarsening and transformation of carbides, together with the substantial reduction in carbon supersaturation of the ferritic matrix, significantly decreases the lattice microstrain. The resulting reduction in internal stresses facilitates the formation of subgrain and domain boundaries, leading to a measurable refinement of the coherent diffraction domains and, consequently, a reduction in the apparent crystallite size. This behaviour is fully consistent with the microstructural evolution expected during long-term thermal ageing of low-alloy Cr–Mo bainitic steels.

The phase transformations identified by X-ray diffraction in the investigated 10H2M steel also affected the texture coefficient (TC) (Fig. 15), calculated according to the Harris relation (Eq. (10)) [46]:

$$TC_{(hkl)} = \frac{\frac{I_{(hkl)}}{I^0_{(hkl)}}}{\frac{1}{N}\sum\frac{I_{(hkl)}}{I^0_{(hkl)}}} \tag{10}$$

where, $I_{(hkl)}$ is the measured intensity of the diffraction peak corresponding to the (hkl) crystallographic plane, $I^0_{(hkl)}$ is the standard (reference) intensity of the corresponding plane and N is the total number of diffraction peaks considered in the analysis.

The Harris texture coefficient provides a quantitative measure of the preferred crystallographic orientation and, consequently, identifies the crystallographic planes most favourably oriented for dislocation glide. A value of TC = 1 indicates a random crystallographic orientation, whereas values exceeding unity reflect the presence of preferred texture. In the investigated material, plastic deformation of the ferritic matrix occurs predominantly on the {110} family of crystallographic planes, which is characteristic of body-centred cubic (BCC) crystal structures. However, it is noteworthy that the TC{110} value for the service-exposed specimens is significantly higher than that of the as-received material. This behaviour can be directly associated with the reduced carbon supersaturation of the bainitic ferrite following prolonged service exposure (Fig. 13). Carbon depletion decreases the lattice distortion and, consequently, lowers the magnitude of Type II residual microstresses (Fig. 14e), thereby reducing the resistance to dislocation nucleation and glide. As a result, plastic deformation in the service-exposed material becomes increasingly concentrated on the energetically most favourable {110}<111> slip system, leading to a more pronounced crystallographic texture. In contrast, the as-received material, characterised by a higher carbon supersaturation and a fine dispersion of cementite precipitates, exhibits substantially greater resistance to dislocation motion due to more effective defect pinning (Fig. 15b). This behaviour is reflected not only in its higher yield strength (Table 1), but also in the more rapid decrease of the TC{110} coefficient during deformation, indicating the earlier activation of secondary slip systems. The progressive operation of multiple slip systems promotes enhanced work hardening, which explains the lower ductility observed during monotonic tensile testing (Fig. 3a). At the same time, the increased resistance to dislocation motion delays cyclic plastic strain accumulation, resulting in a higher fatigue life (N_f) at a given applied stress amplitude (σ_a) compared with the service-exposed material.

3.6. EBSD-informed RVE simulation and stress concentration analysis

3.6.1. RVE construction and mesh discretisation

To rigorously validate the microstructural degradation mechanisms proposed in Sections 3.3-3.5, a physically grounded finite-element framework was employed. EBSD-informed two-phase representative volume elements (RVEs) were constructed for both the as-received and prolonged-service material conditions. The simulations were further used to investigate whether the size-dependent fatigue initiation transition recently established for hierarchical additively manufactured alloys by Capaldi et al. [47] also governs degradation in service-exposed 10H2M steel.

Fig. 16 presents the resulting two-phase RVE geometries after EBSD segmentation and Voronoi tessellation, visually confirming the substantially denser and more boundary-clustered cementite distribution in the prolonged-service condition relative to the as-received microstructure.

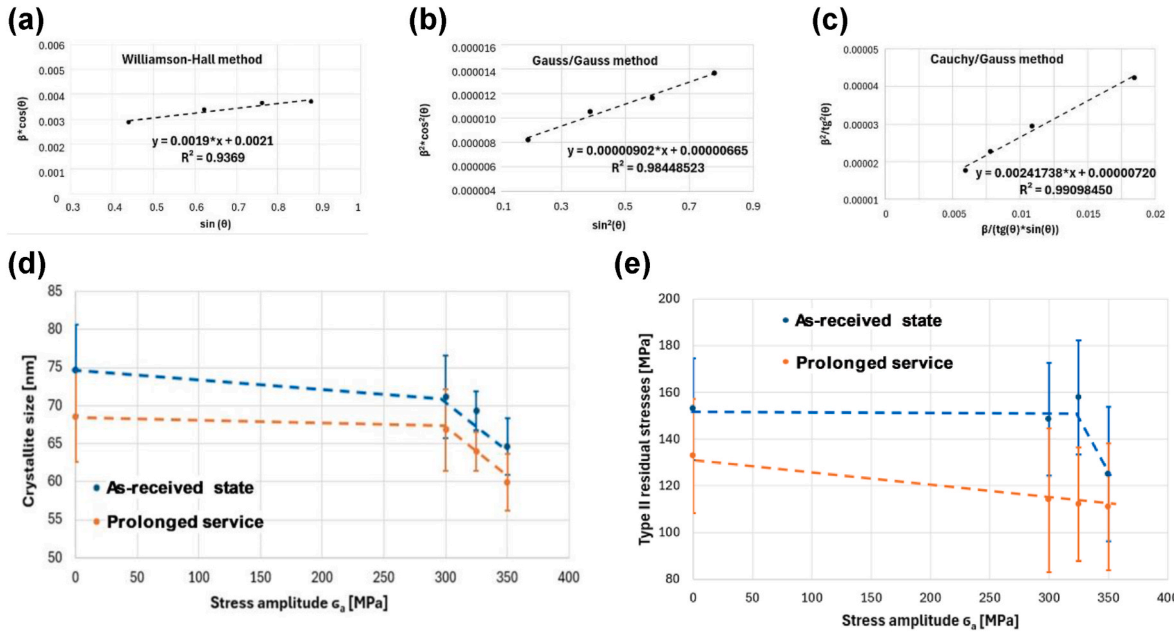

Fig. 14. Methodology for determining the crystallite size (D) and Type II residual (micro-) stress using the Williamson–Hall (a), Gauss/Gauss (b), and Cauchy/Gauss (c) line-profile analysis methods, demonstrated for a non-deformed specimen after prolonged service. The corresponding average values of the ferritic matrix crystallite size (d) and Type II residual stress (e).

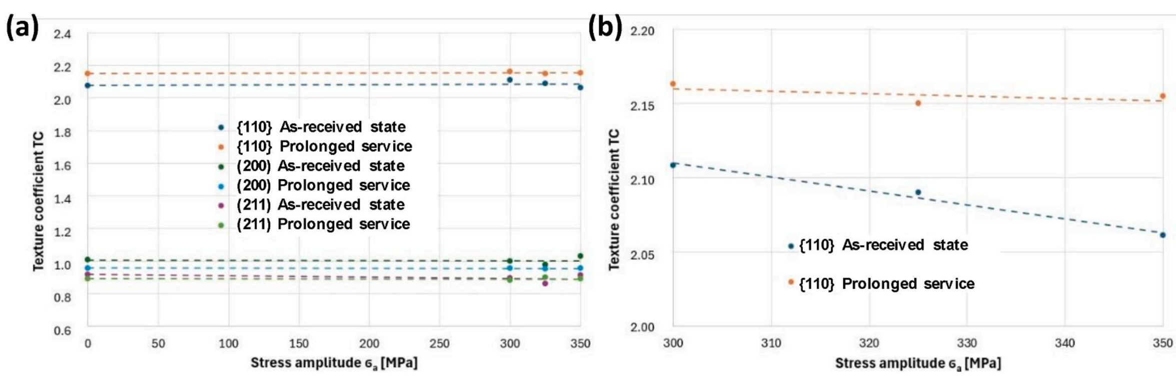

Fig. 15. Texture coefficient (TC) values determined for the identified crystallographic planes of 10H2M steel in the as-received and prolonged-service conditions (a), together with the evolution of the TC{110} coefficient as a function of the applied stress amplitude (σ_a) for both material states (b).

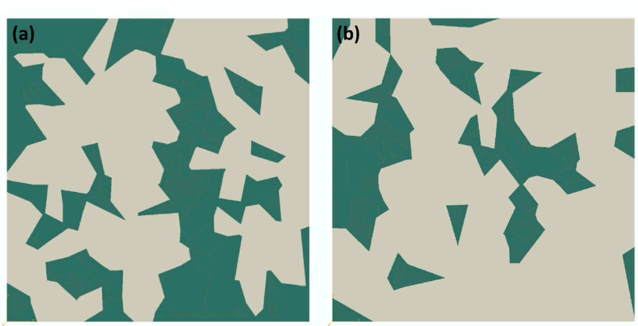

Fig. 16. Two-phase EBSD-informed RVE models showing the Voronoi-tessellated matrix (grey) and cementite (highlighted) phases for as-received (a) and prolonged-service 10H2M steel (b), both at an identical domain size of 43.3 × 43.3 μm^2.

EBSD phase maps were converted into statistically representative Voronoi tessellations (Neper) and discretised into quadratic plane-strain triangular elements (CPE6) at an identical domain size for both conditions, isolating microstructural evolution as the sole independent variable. The associated mesh and EBSD maps are listed in Table 3. This local RVE-based carbide fraction shown earlier as 23.2% to 41.2%, a 1.78-fold increase, is fully consistent, within expected sampling variability between localised RVE domains and bulk-averaged phase maps, with the independent bulk EBSD carbide quantification already reported (Fig. 11; 7.9% to 17.9%, a 2.27 times increase). Both measurements obtained via distinct segmentation methods at different length scales converge on the same physical conclusion, i.e. carbide area fraction

Table 3
Mesh discretisation and phase statistics of the EBSD-informed two-phase representative volume elements (RVEs) constructed for the as-received and prolonged-service 10H2M steel conditions at an identical domain size.

Parameter	As-Received RVE	Prolonged-service RVE
Domain size	43.3 × 43.3 μm^2	43.3 × 43.3 μm^2
Total nodes	43,472	67,199
Total elements (CPE6)	21,549	33,370
Total grain/facet count	103	149
Cementite facets	46	98
Cementite area fraction (RVE-local)	23.2%	41.2%

approximately doubles after 280,000 h of service, corroborating the coarsening or redistribution mechanism established via Ostwald ripening kinetics [36,37] discussed in Section 3.4.

3.6.2. Constitutive modelling and finite-element loading

Each phase was governed by a dedicated user subroutine (UMAT) J_2 radial-return plasticity for the matrix (calibrated directly against the tensile curves in Table 1, using true stress–plastic strain data extracted from Fig. 3a), and linear elasticity for cementite. Uniaxial displacement-controlled loading was applied to both RVEs, with reaction forces (RF1) extracted at the loading boundary. The corresponding von Mises stress distributions obtained from finite-element loading of both RVEs are presented in Fig. 17, with zoomed insets highlighting the precise location of peak stress concentration at the carbide–matrix interfaces used to compute stress concentration factor (K_t) in Table 4. It is acknowledged that present calibration implicitly assumes the matrix phase within the RVE and finite element loading was performed using experimentally obtained tensile properties of bulk alloy. Microstructural heterogeneity arising from dislocation pile-up and pinning effects at carbide vicinity cannot be explicitly resolved by the present single crystal independent J_2 plasticity formulation. Henceforth, the absolute magnitude of $\sigma_{\max,local}$ should be considered as a lower bound estimation methodology for true interfacial stress concentration. However, relative increase in K_t value between the as-received and prolonged-service conditions, which isolates microstructural evolution as the sole variable remains a robust comparative metric.

Table 4
Finite-element reaction force, homogenised nominal stress, peak local von Mises stress, and resulting stress concentration factor (K_t) for the as-received and prolonged-service RVEs, validated against the experimentally measured ultimate tensile strength (Table 1).

Quantity	As-Received	Prolonged service
Reaction Force	22,453 N	18,232 N
$\sigma_{nominal}$	518.55 MPa	421.06 MPa
$\sigma_{max,local}$ (peak interfacial von Mises)	554.9 MPa	548.0 MPa
Stress Concentration factor, K_t	1.070	1.301

3.6.3. Local stress concentration factor (K_t)

The nominal (homogenised) stress and local stress concentration factor were computed as:

$$\sigma_{nominal} = \frac{RF_1}{A} \tag{11}$$

$$K_t = \frac{\sigma_{max,local}}{\sigma_{nominal}} \tag{12}$$

where A = 43.3 μm^2 is the fixed RVE cross-section (identical for both conditions) and $\boldsymbol{\sigma_{max,local}}$ is the peak von Mises stress extracted at the carbide–matrix interface.

Both $\sigma_{nominal}$ values obtained from RVE-simulation remain below the experimentally measured tensile strength, confirming the simulations captured physically realistic post-yield plastic deformation consistent with the tensile response reported in Table 1, rather than an arbitrary

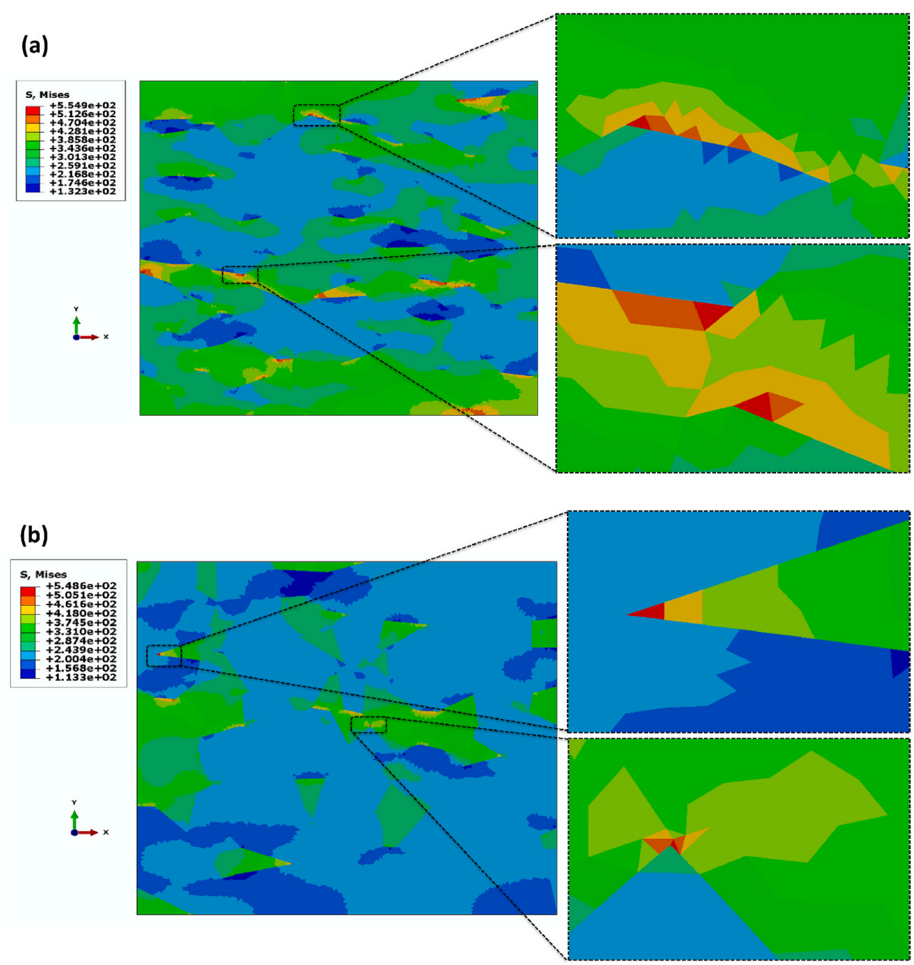

Fig. 17. Von Mises stress contour plots from finite-element loading of the two-phase RVEs for as-received (a) and prolonged-service 10H2M steel (b), with zoomed insets showing the local stress concentration zones at the carbide–matrix interfaces used to determine the peak stress.

overload state. The resulting 21.6% increase in K_t after prolonged service from 1.070 to 1.301 provides direct micromechanical corroboration of the 25.7% reduction in yield strength measured experimentally (334 to 248 MPa as listed in Table 1), confirming that carbide-scale stress amplification is a primary contributor to the macroscopic strength loss.

3.6.4. Testing the size-dependence hypothesis

Capaldi et al. [47] demonstrated that fatigue crack initiation mechanisms transition between structural tiers when the governing microstructural length scale, ξ, becomes comparable to the specimen or plastic-zone dimension in their nanolamellar high-entropy alloy, ξ shifted three orders of magnitude (263 nm at the nanolamellar scale to 213 μm at the melt-pool-boundary scale) depending on which hierarchical tier dominated at a given specimen size. To rigorously test whether an analogous size-dependent transition governs fatigue initiation in 10H2M steel, the mean inter-carbide spacing, λ, was computed using the standard random-dispersion relation:

$$\lambda = \overline{d}_{cem}\sqrt{\frac{\pi}{4f_{cem}}} \tag{13}$$

where $\overline{d}_{cem}$ is the mean cementite equivalent diameter and f_{cem} is the local cementite area fraction.

Here, Table 5 shows both results and compares them against the fixed RVE domain size, $L = 43.3$ μm. Because L was held constant across both simulations, the 31.5% reduction in λ from 6.38 to 4.37 μm and the corresponding increase in L/λ from 6.8 to 9.9 isolate carbide-scale spacing evolution, not a change in the governing structural length scale as the sole driver of the 21.6% K_t increase. Unlike the melt-pool boundary controlled macroscale transition identified by Capaldi et al. [47] for additive manufactured alloys, 10H2M steel exhibits no evidence of a specimen's size-dependent shift in its fatigue initiation mechanism using fixed RVE domain size (43.3 × 43.3 μm^2) investigated in the present study. Instead, degradation manifests as a progressive intensification of local stress concentration within a single, carbide-interface-dominated initiation regime fully consistent with the fractographic conclusion (Section 3.3) stating that prolonged exposure does not fundamentally change the surface-dominated initiation mechanism but intensifies the role of carbides and boundary-related defects.

4. Discussion

4.1. Effect of prolonged service on load-bearing capacity

The mechanical response presented in Fig. 3a and Table 1 demonstrates that prolonged service primarily affects the resistance of 10H2M steel to the onset of plastic deformation rather than its ultimate load-bearing capacity. After 280,000 h of service at 540 °C, the yield strength decreased approximately 26%, whereas the ultimate tensile strength remains nearly unchanged. These results indicate that prolonged service substantially reduces the stress required to initiate macroscopic plastic deformation, while the material retains its ability to carry load and undergo further plastic deformation before final failure. The reduction in yield strength after prolonged service is primarily associated with the service-induced evolution of the ferritic-bainitic microstructure. As shown in Fig. 1, the as-received material exhibits packets of lath- or plate-shaped ferrite characteristic of the initial ferritic-bainitic structure, whereas prolonged exposure promotes precipitation and redistribution of carbides from the primary bainitic microstructure, with increased carbide accumulation particularly along boundaries. Quantitative carbide analysis further supports this evolution, showing an increase in carbide area fraction from approximately 7.9% in the non-deformed as-received material to 17.9% after prolonged service, together with pronounced carbide coarsening and accumulation along grain boundaries, packet boundaries and lath interfaces. Similar microstructural degradation during long-term high-temperature exposure has been reported for creep-resistant X20CrMoV12.1 steel [36] and 2.25Cr–1Mo low-alloy ferritic steel [37], where prolonged thermal exposure promotes dissolution of fine intragranular carbides and preferential growth and agglomeration of coarse carbides along grain boundaries.

From the viewpoint of strengthening mechanisms, the initial fine dispersion of carbides provides numerous barriers to dislocation motion and therefore contributes to the higher resistance to plastic yielding of the as-received material. During prolonged thermal exposure, diffusion-driven carbide coarsening reduces the effectiveness of this fine precipitate distribution, while redistribution of carbon from the bainitic ferrite toward carbide phases decreases the contribution of solid-solution strengthening. Simultaneously, carbide coarsening increases the interparticle spacing, allowing dislocations to move more readily during the initial stages of plastic deformation. The XRD analysis supports this interpretation by showing that the estimated carbon concentration in the supersaturated ferritic matrix decreases from approximately 0.22 wt % in the as-received condition to 0.08 wt% after prolonged service. Additionally, the prolonged-service material exhibits reduced Type II residual microstress together with a decrease in crystallite size compared with the as-received condition (Fig. 14), indicating relaxation of the highly strained initial microstructural state during prolonged thermal exposure. Therefore, the lower yield strength after service can be attributed to the combined effects of carbon depletion, carbide precipitation and coarsening, redistribution of strengthening particles, and relaxation of the internal microstress state.

Despite these changes, the ultimate tensile strength remains almost unchanged. This suggests that the underlying ferritic-bainitic matrix retains substantial load-bearing and strain-hardening capability after prolonged service. Once yielding has initiated, progressive dislocation multiplication and interactions within the matrix can continue to accommodate plastic deformation, allowing the prolonged-service material to sustain increasing applied stress comparable to that of the as-received material.

Although the monotonic tensile properties exhibited only a moderate reduction after prolonged service, the VHCF strength deteriorated much more significantly. This difference indicates that the mechanisms controlling monotonic yielding and fatigue crack initiation are fundamentally different. Monotonic deformation depends primarily on the average resistance of the microstructure to dislocation motion, whereas VHCF behaviour is governed by local stress concentrations and cyclic strain localisation. Consequently, relatively small microstructural changes produced during service can have only a limited influence on the global load-bearing capacity while simultaneously causing a substantial reduction in fatigue resistance.

4.2. Microstructure-controlled fatigue damage evolution

The pronounced reduction in fatigue life shown by the S–N curves (Fig. 3b) is governed primarily by the evolution of the microstructure during prolonged service and its influence on the localisation of cyclic plastic deformation. The contribution of grain boundaries to fatigue behaviour was evaluated using the grain boundary distributions presented in Table 6. In the non-deformed as-received material, the microstructure is characterised by a high fraction of high-angle

Table 5
Mean inter-carbide spacing (λ) and RVE domain-to-spacing ratio (L/λ) for the as-received and prolonged-service conditions, evaluated using the size-dependent fatigue initiation framework to assess whether a specimen-size-dependent mechanistic transition governs crack initiation in 10H2M steel.

Length-scale parameter	As-Received	Prolonged service
Inter-carbide spacing, λ (Eq. (13))	6.38 μm	4.37 μm
RVE domain size, L (fixed)	43.3 μm	43.3 μm
L/λ ratio	6.8	9.9
K_t	1.070	1.301

Table 6
Distribution of LABs and HABs in the non-deformed state and after ultrasonic fatigue testing.

Specimen Condition	Misorientation angle	As-received	Prolonged service
Non-deformed	2°-5°	0.126	0.200
	5°-15°	0.026	0.030
	15°-180°	0.847	0.769
After fatigue (300 MPa)	2°-5°	0.141	0.065
	5°-15°	0.032	0.035
	15°-180°	0.827	0.900
After fatigue (350 MPa)	2°-5°	0.115	0.092
	5°-15°	0.030	0.054
	15°-180°	0.855	0.854

boundaries (HABs) equal to approximately 85%, while the fraction of low-angle grain boundaries (LABs) remains relatively small. This boundary distribution contributes to a more homogeneous deformation of the material during cyclic loading. It is consistent with the relatively uniform transgranular crack propagation observed in the fracture surfaces (Fig. 6). The high fraction of HABs acts as an effective barrier to dislocation motion, forcing the propagating crack to change its propagation direction repeatedly and thereby delaying fatigue crack growth. On the other hand, in specimens after prolonged service, the fraction of HABs remains high and even reaches approximately 90% for specimens tested at 300 MPa. However, it does not result in improved fatigue resistance. One should highlight that the prolonged exposure at elevated temperature promotes carbide precipitation and coarsening preferentially along grain and packet boundaries [36,37], reducing their ability to accommodate cyclic deformation. Consequently, these interfaces become regions of local stress concentration where dislocations accumulate during cyclic loading. This was further confirmed by the increased local misorientation observed in the KAM maps (Fig. 8).

The EBSD parameters summarised in Table 6 show a clear dependence on the applied stress amplitude during ultrasonic fatigue testing. With increasing stress amplitude, a systematic increase in the fraction of regions exhibiting elevated local misorientation can be observed. This trend is reflected in the higher kernel average misorientation (KAM) values measured in specimens tested at higher stress levels. Since KAM is directly related to the density of geometrically necessary dislocations (GNDs), the observed increase indicates a progressive accumulation of plastic strain within the microstructure as the cyclic stress amplitude increases. At lower stress amplitudes, corresponding to the very-high-cycle fatigue regime, the EBSD maps reveal relatively low misorientation values and a microstructure dominated by LABs. Under these conditions, plastic deformation is highly localised and primarily occurs near microstructural heterogeneities such as carbide particles or grain boundaries. As the stress amplitude increases, a gradual increase in the proportion of HABs can be observed in Table 6. This effect suggests that elevated strain energy accumulated due to cyclic deformation promotes subgrain rotation and the transformation of low-angle subgrain boundaries into higher-angle interfaces due to progressive dislocation rearrangement [48].

The influence of long-term exposure becomes particularly evident when these trends are compared between the as-received and the prolonged-service material. In the steel after long-term operation, the increase in KAM values with stress amplitude is more pronounced. This behaviour indicates that the degraded microstructure exhibits a greater tendency toward localised plastic strain accumulation under cyclic loading [2]. The enhanced strain localisation can be attributed primarily to the coarsening and redistribution of carbide precipitates during service.

Carbide particles play a critical role in controlling the deformation behaviour of 10H2M steel. In the as-received material, the relatively fine and uniformly distributed carbides act as effective obstacles to dislocation motion, promoting a more homogeneous distribution of plastic strain. However, prolonged service at elevated temperature leads to carbide coarsening and partial segregation along grain and packet boundaries. The reduction in particle number density and the increase in carbide size create stronger local stress concentrations around these particles. As a result, when the material is subjected to higher cyclic stress amplitudes, dislocations tend to accumulate around the coarse carbides, forming local pile-ups and increasing lattice curvature in their vicinity. These effects are clearly reflected in the EBSD results, where regions surrounding carbide particles exhibit significantly higher local misorientation values compared with the surrounding matrix. Consequently, the EBSD parameters listed in Table 6 show a stronger sensitivity to stress amplitude in the prolonged-service material.

The combined influence of increased stress amplitude and carbide coarsening therefore promotes the development of localised deformation zones. These zones act as preferential sites for fatigue crack initiation, particularly in the very-high-cycle fatigue regime where crack nucleation rather than propagation dominates the fatigue life. The fractographic observations support this interpretation. One should highlight that in both conditions, fatigue cracks initiated near the surface, but in the prolonged-service material, carbides and boundary-related degradation played a more dominant role in nucleation. While crack propagation in the as-received steel was regular and predominantly transgranular, the prolonged-service specimens displayed irregular crack paths, frequent deflections, and mixed fracture features.

Within the investigated stress amplitude range, fatigue cracks consistently initiated at or near the specimen surface in both material conditions. It should be noted that the absence of subsurface crack initiation in the present study does not contradict the VHCF regime. Internal crack initiation is most frequently reported for very-high-strength steels containing large non-metallic inclusions, where the applied stress amplitude is sufficiently low for inclusion-controlled damage to dominate over surface damage [49,50]. In contrast, the investigated 10H2M steel is a ferritic-bainitic Cr-Mo steel with a moderate tensile strength equal to 545 MPa, and fractographic observations did not reveal characteristic fish-eye morphology or fine granular areas (FGAs) associated with internal crack initiation. Instead, fatigue cracks consistently originated at or near the specimen surface, where carbides, carbide clusters and local surface imperfections acted as preferential stress concentrators. In the prolonged-service material, long-term exposure at 540 °C promoted carbide coarsening and redistribution along grain and packet boundaries, further increasing the susceptibility of the surface region to crack nucleation. Therefore, although the specimens were tested up to 10^9 cycles, the dominant fatigue crack initiation mechanism remained surface-controlled rather than inclusion-controlled. The schematic of fatigue crack propagation under USF conditions is presented in Fig. 18. A similar fatigue crack initiation mechanism from surface or near-surface defects in the VHCF regime has been reported for SLM-produced AlSi12 alloy with a tensile strength of approximately 390 MPa [12].

It is worth emphasising that the evolution of carbides during prolonged service changes the local mechanical response of the microstructure due to the elastic mismatch between the hard carbide particles and the soft ferritic matrix [51]. Although atomic-scale characterisation techniques, such as 4D scanning transmission electron microscopy (4D-STEM), were not employed in the present study, the observed microstructural evolution can be interpreted based on the established elastic properties of the constituent phases. Carbide particles possess substantially higher stiffness, bulk modulus and shear modulus than the surrounding ferritic matrix. Consequently, prolonged service-induced carbide coarsening enhances the elastic mismatch at the carbide/matrix interfaces, particularly along grain and packet boundaries where coarse carbides preferentially precipitate. Under cyclic loading, this mismatch promotes local stress concentration and restricts the accommodation of plastic deformation, leading to dislocation accumulation and localised lattice distortion. This interpretation is consistent with the increased local misorientation observed in the KAM maps of the

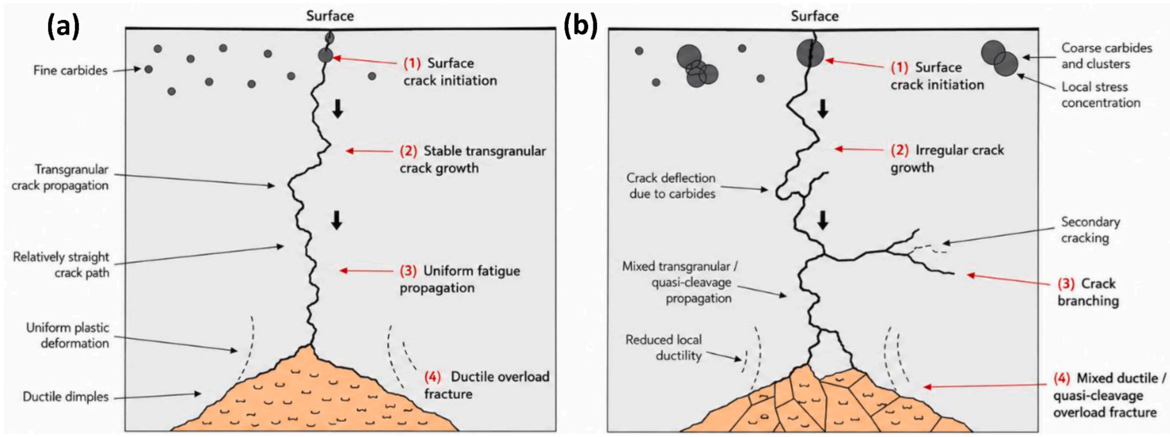

Fig. 18. Schematics of crack propagation in as-received (a) and prolonged-service (b) 10H2M steel during ultrasonic fatigue testing.

prolonged-service material. The resulting strain localisation facilitates fatigue crack initiation at carbide-rich grain boundaries, in agreement with the fractographic observations. In contrast, the finer and more uniformly distributed carbides in the as-received material reduce the local stiffness mismatch, resulting in a more homogeneous distribution of cyclic strain and improved fatigue resistance.

4.3. *Thermal signature as indirect evidence of localised vs. distributed plasticity*

The temperature evolution recorded during ultrasonic fatigue testing provides additional insight into the mechanical response of 10H2M steel, complementing the tensile data (Fig. 3a), S-N curves (Fig. 3b), and temperature histories (Figs. 4 and 5). Although the applied cooling strategy successfully kept the global specimen temperature below 30 °C during most of the test, some thermal changes still developed during each loading cycle. In the as-received material, temperature increases during each 110 ms loading pulse were observed. At amplitudes around 350–375 MPa, the temperature increased by several degrees during each loading cycle (Fig. 5), indicating consistent energy dissipation through local plastic deformation [52]. As cycling progressed, the temperature exhibited a gradual upward trend followed by a sudden, sharp increase immediately prior to failure, with peak temperatures reaching 80–120 °C depending on amplitude (Table 2). These pronounced thermal changes suggest that the as-received microstructure accommodates significant plasticity near the crack tip throughout most of the fatigue life. This agrees with the fractographic observations, where the fatigue crack propagated in a relatively uniform transgranular manner and the final overload fracture displayed mixed ductile morphology. The elevated thermal response is therefore characteristic of a steel capable of sustaining and dissipating cyclic strain energy over long durations, consistent with its extended VHCF lives. On the other hand, the steel after prolonged service behaved noticeably differently. Temperature rises during pulses were smaller and less uniform, and the final temperature peaks recorded at fracture were consistently lower than those of as-received specimens at the same stress amplitudes (Table 2). This reduced thermal signature indicates limited microplasticity during crack growth. The coarsening and segregation of carbides observed in the prolonged-service microstructure (Fig. 1b) likely inhibit the plastic deformation that can occur around a propagating crack, promoting more abrupt and brittle-like advance with reduced heat generation. This interpretation aligns with the fractography, which revealed irregular crack paths, quasi-cleavage facets, and frequent deflections. This behaviour suggests that the degraded microstructure stores less energy in the form of distributed plastic deformation and instead concentrates deformation within a limited number of highly stressed regions surrounding coarse carbides and grain boundaries [53]. Once a fatigue crack nucleates at these preferential sites, crack propagation requires relatively limited additional plastic deformation in the surrounding matrix. Consequently, failure occurs after less cumulative plastic deformation, which is reflected by the lower temperatures measured during ultrasonic fatigue testing. The thermal response therefore provides indirect evidence that long-term service changes the fatigue damage mechanism from relatively homogeneous cyclic plasticity to increasingly localised damage controlled by carbide-induced stress concentrations.

4.4. *Multiscale correlation between XRD, EBSD and RVE*

The degradation mechanism of 10H2M steel after prolonged high-temperature service can be consistently interpreted by integrating the results obtained from XRD, EBSD and EBSD-informed finite-element RVE simulations. Although each technique characterises the material at a different length scale, all three provide complementary evidence that prolonged service modifies the microstructure in a manner that promotes localised cyclic deformation and consequently reduces fatigue resistance.

The XRD analysis (Figs. 12–15) reveals thermodynamically driven carbide precipitation together with carbon depletion and residual stress relaxation. The precipitation of carbides from the primary bainitic microstructure during long-term exposure at 540 °C is driven by the reduction of the Gibbs free energy (ΔG) of the supersaturated solid solution. The thermodynamic driving force for precipitation may be expressed as:

$$\Delta \mathrm{G} = \Delta \mathrm{H} - \mathrm{T}\Delta \mathrm{S} \tag{14}$$

where, ΔH is the enthalpy change associated with carbide formation, ΔS is the entropy change and T is the absolute temperature.

For diffusion-controlled precipitation, the chemical driving force can also be expressed as the Gibbs free energy change per unit volume (ΔG_v):

$$\Delta \mathrm{G}_v = \frac{\mathrm{RT}}{V_m} \Big/ \ln\left(\frac{C}{C_{eq}}\right) \tag{15}$$

where, R is the gas constant, T is the absolute temperature, V_m is the molar volume, C is the carbon concentration within the supersaturated bainitic matrix and C_{eq} is the equilibrium solubility at the service temperature.

The total free energy associated with carbide nucleation is given by:

$$\Delta \mathrm{G}_{total} = \Delta \mathrm{G}_v + \gamma A + E_{strain} \tag{16}$$

where, γ represents the interfacial energy between the carbide and ferritic matrix, A denotes the interfacial area and E_{strain} is the elastic strain energy arising from lattice misfit. During prolonged thermal exposure, diffusion gradually reduces the chemical supersaturation while Ostwald ripening decreases the total interfacial energy by replacing numerous fine precipitates with fewer coarse carbides. This evolution is consistent with the coarse carbide population observed after prolonged service and explains the increasing tendency for stress localisation and fatigue crack initiation at carbide-rich interfaces.

The occurrence of precipitation processes and carbide coarsening through the Ostwald ripening mechanism within the supersaturated bainitic ferrite matrix was further confirmed by X-ray diffraction (XRD) phase analysis performed on both the as-received and prolonged-service specimens (Fig. 12). The diffraction patterns further confirmed that, irrespective of the applied stress amplitude, the as-received material consists predominantly of a ferritic matrix accompanied by low-intensity diffraction peaks attributed to cementite (Fe_3C). Following prolonged service exposure of the investigated 10H2M steel, pronounced microstructural evolution occurred, as illustrated in Fig. 12. This phenomenon is commonly referred to as Ostwald ripening [38,39] and involves the precipitation and coarsening of carbides from the supersaturated bainitic ferrite, preferentially along grain boundaries, accompanied by the thermodynamically driven carbide sequence $M_3C \rightarrow M_7C_3 \rightarrow M_{23}C_6$ [40]. Considering the chromium content of the investigated steel, this transformation proceeds through the gradual replacement of cementite (Fe_3C) by chromium-rich carbides ($Cr_{23}C_6$). The driving force for this process arises from the substantially lower Gibbs free energy of formation (ΔG) of $Cr_{23}C_6$, amounting to -344 kJ mol^{-1} at 298 K [54], compared with approximately $+20$ kJ mol^{-1} for cementite [55]. Consequently, chromium carbide precipitation represents the thermodynamically preferred state during long-term thermal exposure.

The EBSD analysis (Figs. 7–9 and Table 6) further demonstrates that the carbide area fraction increases from approximately 7.9% in the as-received condition to 17.9% after prolonged service, accompanied by preferential carbide accumulation along grain and sub-grain boundaries, higher KAM values and increased GND density. These observations indicate that the service-induced microstructural evolution progressively changes the deformation behaviour from relatively homogeneous plastic flow to highly localised cyclic deformation. Similar carbide coarsening and grain-boundary enrichment during long-term thermal exposure have been reported for creep-resistant Cr–Mo steels by Godec and Skobir Balantič [36] and Yang et al. [37], where diffusion-controlled precipitation and Ostwald ripening govern the degradation of the bainitic microstructure.

The RVE simulations provide quantitative micromechanical support for these experimental observations. Using the carbide distributions extracted directly from the EBSD maps, the simulations demonstrate that carbide coarsening significantly increases stress localisation at the carbide/matrix interfaces, increasing the local stress concentration factor from 1.070 for the as-received material to 1.301 after prolonged service. This increase agrees well with the higher KAM values measured experimentally and confirms that the coarse carbides and carbide-enriched grain boundaries become preferential sites for strain accumulation during cyclic loading. Consequently, although fatigue cracks initiate from the surface in both material conditions (Fig. 6), the prolonged-service material exhibits accelerated crack nucleation because the local stress concentration around carbide-rich regions is substantially enhanced. These local micromechanical changes dominate the fatigue response, providing a physically consistent explanation for the pronounced deterioration in VHCF resistance of the prolonged-service 10H2M steel.

4.5. Implications for remaining life assessment

The results obtained in this study have practical implications for the remaining life assessment (RLA) of high-temperature power plant components manufactured from 10H2M steel. The comparison between the VHCF behaviour of the as-received and prolonged-service materials provides a quantitative measure of the degradation in fatigue performance resulting from prolonged service exposure. Such information can complement existing RLA methodologies, which are primarily based on creep damage assessment, tensile testing, hardness measurements and metallographic examination [56–58]. The present study demonstrates that prolonged service at elevated temperature leads to a significant reduction in VHCF resistance despite only a moderate decrease in the standard tensile properties. This finding suggests that evaluation of the conventional mechanical properties alone may not adequately reflect the residual resistance of aged components subjected to long-term cyclic loading. Therefore, the VHCF data obtained in this study can provide an additional material parameter in practical RLA procedures for assessing components subjected to a very large number of low-amplitude cyclic loading events, such as those associated with turbine start-up/shut-down cycles, flow-induced vibrations, pressure fluctuations or other operational dynamic loading. Additionally, the observed transition toward more pronounced carbide-controlled surface crack initiation provides a microstructural indicator of fatigue degradation that can support inspection planning and fracture-mechanics-based remaining life evaluations of long-term operated power plant components.

5. Conclusions

The main conclusions of the presented research were as follows:

- Long-term service at elevated temperature caused only a moderate decrease in the yield strength of 10H2M steel, while ultimate tensile strength and ductility remained largely unchanged.
- Despite the limited effect on static properties, fatigue response in the VHCF regime was substantially reduced in the prolonged-service material across all applied stress amplitudes.
- Fractographic analysis showed that fatigue cracks in both as-received and prolonged-service 10H2M steels initiated near the surface, with carbides serving as the dominant crack nucleation sites under VHCF loading. The coarsening of near-surface carbides during service accelerates crack initiation and growth, ultimately reducing the fatigue life of critical components.
- In the as-received state, cracks propagated in a relatively uniform transgranular manner, while in the prolonged-service steel, carbide coarsening promoted irregular crack paths, secondary cracking, and mixed transgranular/quasi-cleavage features. Final overload fracture was ductile in the as-received condition, but in the prolonged-service material, it was accompanied by quasi-cleavage facets, reflecting reduced local ductility after prolonged service.
- EBSD-informed finite-element RVE simulations demonstrated that prolonged service exposure increased the local carbide/matrix stress concentration factor (K_t) from 1.070 to 1.301 owing to carbide coarsening and reduced inter-carbide spacing. The simulations further confirmed that fatigue crack initiation remained governed by a carbide-interface-dominated mechanism, without evidence of a specimen-size-dependent transition in the governing initiation mechanism.
- XRD analysis confirmed that prolonged service exposure promoted thermodynamically driven carbide precipitation and Ostwald ripening, resulting in carbon depletion of the bainitic ferrite, crystallite refinement, reduced Type II residual microstress and enhanced {110} texture. These microstructural changes reduced resistance to cyclic plastic deformation and contributed to the deterioration of the VHCF performance of the investigated 10H2M steel.

CRediT authorship contribution statement

Ved Prakash Dubey: Data curation, Formal analysis, Investigation, Methodology, Writing – review & editing. **Marzena Pawlik:** Data curation, Investigation, Methodology, Writing – original draft.

Dominika Przygucka: Investigation. **Pankaj Kumar:** Formal analysis, Investigation, Methodology, Writing – original draft. **Stanisław Jóźwiak:** Formal analysis, Investigation, Methodology, Writing – original draft. **Zbigniew L. Kowalewski:** Validation, Writing – review & editing. **Paul Wood:** Formal analysis, Investigation, Methodology, Project administration, Validation, Writing – review & editing. **Mateusz Kopec:** Conceptualization, Formal analysis, Investigation, Methodology, Project administration, Supervision, Validation, Visualization, Writing – original draft, Writing – review & editing.

Declaration of competing interests

The authors declare that they have no known competing financial interests or personal relationships that could have appeared to influence the work reported in this paper.

Acknowledgements

The authors would like to express their gratitude to Mr Wayne Carter and Mr Trevor Wright for their kind help during the experimental part of this work. This work was funded by the College of Science and Engineering, University of Derby. Mr V.P. Dubey's work was financially supported by the Foundation for Polish Science START award.

Data availability

Data will be made available on request.

References

[1] M. Gwoździk, M. Motylenko, D. Rafaja, Microstructure changes responsible for the degradation of the 10CrMo9-10 and 13CrMo4-5 steels during long-term operation, Mater. Res. Express 7 (2020) 016515, https://doi.org/10.1088/2053-1591/ab5fc8.
[2] M. Kopec, The analysis of strain response for as-received and exploited 10H2M power engineering steel subjected to low cycle fatigue in plastic regime, Int. J. Pres. Ves. Pip. 207 (2024) 105110, https://doi.org/10.1016/j.ijpvp.2023.105110.
[3] T. Wang, J. Gao, S. Li, J. Li, J. Li, H. Bu, H. Qi, Z. Li, M. Li, Microstructure evolution and mechanical properties degradation behavior of nuclear power pressure vessel steel induced by prolonged thermal aging, J. Mater. Res. Technol. 34 (2025) 2740–2753, https://doi.org/10.1016/j.jmrt.2024.12.243.
[4] S. Ma, S. Han, X. Li, Y. Li, C. Wang, Investigation of high-temperature durability and microstructure evolution of G115 steel after long-term aging at 650 °C, Metals 15 (2025) 535, https://doi.org/10.3390/met15050535.
[5] Y. Gorash, T. Comlekci, C. Walker, A. Toumpis, J. Kelly, A. England, L. Milne, Comparative fatigue analysis of structural steels considering welding and surface effects, Strain 61 (2025) e70003, https://doi.org/10.1111/str.70003.
[6] H. Mayer, Recent developments in ultrasonic fatigue, Fatig. Fract. Eng. Mater. Struct. 39 (2016) 3–29, https://doi.org/10.1111/ffe.12365.
[7] M. Manjunatha, Y. Gorash, T. Comlekci, L. Milne, D. Mackenzie, Very high cycle fatigue and fatigue crack growth of steels: a review, Appl. Sci. 16 (2026) 1737, https://doi.org/10.3390/app16041737.
[8] R. Caivano, A. Tridello, G. Chiandussi, G. Qian, D. Paolino, F. Berto, Very high cycle fatigue (VHCF) response of additively manufactured materials: a review, Fatig. Fract. Eng. Mater. Struct. 44 (2021) 2919–2943, https://doi.org/10.1111/ffe.13567.
[9] Q. Pan, L. Lu, Fatigue in metals and alloys, Nat. Mater. 25 (2026) 357–365, https://doi.org/10.1038/s41563-025-02308-5.
[10] J. Günther, D. Krewerth, T. Lippmann, S. Leuders, T. Tröster, A. Weidner, H. Biermann, T. Niendorf, Fatigue life of additively manufactured Ti–6Al–4V in the very high cycle fatigue regime, Int. J. Fatig. 94 (2017) 236–245, https://doi.org/10.1016/j.ijfatigue.2016.05.018.
[11] A. Tridello, C.A. Biffi, J. Fiocchi, P. Bassani, G. Chiandussi, M. Rossetto, A. Tuissi, D.S. Paolino, VHCF response of as-built SLM AlSi10Mg specimens with large loaded volume, Fatig. Fract. Eng. Mater. Struct. 41 (2018) 1918–1928, https://doi.org/10.1111/ffe.12830.
[12] S. Siddique, M. Imran, F. Walther, Very high cycle fatigue and fatigue crack propagation behavior of selective laser melted AlSi12 alloy, Int. J. Fatig. 94 (2017) 246–254, https://doi.org/10.1016/j.ijfatigue.2016.06.003.
[13] K. Yang, Q. Huang, Q. Wang, Q. Chen, Competing crack initiation behaviors of a laser additively manufactured nickel-based superalloy in high and very high cycle fatigue regimes, Int. J. Fatig. 136 (2020) 105580, https://doi.org/10.1016/j.ijfatigue.2020.105580.
[14] B. Voloskov, S. Evlashin, S. Dagesyan, S. Abaimov, I. Akhatov, I. Sergeichev, Very high cycle fatigue behavior of additively manufactured 316L stainless steel, Materials 13 (2020) 3293, https://doi.org/10.3390/ma13153293.
[15] C. Boursier Niutta, A.P. Pagnoncelli, A. Tridello, J. Fiocchi, C.A. Biffi, A. Tuissi, D. S. Paolino, Very high cycle fatigue (VHCF) response of an additively manufactured nitinol, Int. J. Fatig. 200 (2025) 109130, https://doi.org/10.1016/j.ijfatigue.2025.109130.
[16] Y. Gorash, T. Comlekci, G. Styger, J. Kelly, F. Brownlie, L. Milne, Ultrasonic fatigue testing of structural steel S275JR+AR with insights into corrosion, mean stress and frequency effects, Materials 16 (2023) 1799, https://doi.org/10.3390/ma16051799.
[17] A. England, Y. Gorash, A. Toumpis, Assessing the very high cycle fatigue behavior and frequency effect of structural steel welds, Fatig. Fract. Eng. Mater. Struct. 48 (2025) 1529–1541, https://doi.org/10.1111/ffe.14569.
[18] Y. Gorash, T. Comlekci, C. Walker, J. Kelly, L. Milne, Ultrasonic fatigue testing of welds made of structural steels S355JR and S275JR, Procedia Struct. Integr. 57 (2024) 611–617, https://doi.org/10.1016/j.prostr.2024.03.067.
[19] A. Schmiedel, S. Henkel, T. Kirste, R. Morgenstern, A. Weidner, H. Biermann, Ultrasonic fatigue testing of cast steel G42CrMo4 at elevated temperatures, Fatig. Fract. Eng. Mater. Struct. 43 (2020) 2455–2475, https://doi.org/10.1111/ffe.13316.
[20] I. Marines, Ultrasonic fatigue tests on bearing steel AISI-SAE 52100 at frequency of 20 and 30 kHz, Int. J. Fatig. 25 (2003) 1037–1046, https://doi.org/10.1016/S0142-1123(03)00161-0.
[21] U. Krupp, A. Giertler, K. Koschella, Microscopic damage evolution during very-high-cycle fatigue (VHCF) of tempered martensitic steel, Fatig. Fract. Eng. Mater. Struct. 40 (2017) 1731–1740, https://doi.org/10.1111/ffe.12685.
[22] B. Pyttel, I. Brunner, D. Schwerdt, C. Berger, Influence of defects on fatigue strength and failure mechanisms in the VHCF-region for quenched and tempered steel and nodular cast iron, Int. J. Fatig. 41 (2012) 107–118, https://doi.org/10.1016/j.ijfatigue.2011.10.007.
[23] B.M. Schönbauer, K. Yanase, M. Endo, Influence of intrinsic and artificial defects on the VHCF properties of 17-4PH stainless steel, Procedia Struct. Integr. 2 (2016) 1149–1155, https://doi.org/10.1016/j.prostr.2016.06.147.
[24] J. Trzaska, A. Jagiełło, L. Dobrzański, The calculation of CCT diagrams for engineering steels, Archiv. Mater. Sci. Eng. 39 (2009) 13–20.
[25] M. Szkodo, G. Gajowiec, Studies of the mechanism of metal dusting of 10CrMo9-10 steel after 10 years of operation in the semi-regenerative catalytic reformer, Corros. Sci. 102 (2016) 279–290, https://doi.org/10.1016/j.corsci.2015.10.016.
[26] The Japan Welding Engineering Society. Standard Test Method for Ultrasonic Fatigue Testing of Metallic Materials; WES 1112:2017; the Japan Welding Engineering Society: Tokyo, Japan, 2017, (n.d.).
[27] W. Pantleon, Resolving the geometrically necessary dislocation content by conventional electron backscattering diffraction, Scr. Mater. 58 (2008) 994–997, https://doi.org/10.1016/j.scriptamat.2008.01.050.
[28] Z.Y. Huang, Q.Y. Wang, D. Wagner, C. Bathias, A very high cycle fatigue thermal dissipation investigation for titanium alloy TC4, Mater. Sci. Eng., A 600 (2014) 153–158, https://doi.org/10.1016/j.msea.2014.02.012.
[29] D. Krewerth, T. Lippmann, A. Weidner, H. Biermann, Application of full-surface view *in situ* thermography measurements during ultrasonic fatigue of cast steel G42CrMo4, Int. J. Fatig. 80 (2015) 459–467, https://doi.org/10.1016/j.ijfatigue.2015.07.013.
[30] N.A. Giang, M. Kuna, G. Hütter, Influence of carbide particles on crack initiation and propagation with competing ductile-brittle transition in ferritic steel, Theor. Appl. Fract. Mech. 92 (2017) 89–98, https://doi.org/10.1016/j.tafmec.2017.05.015.
[31] F. Maquin, F. Pierron, Heat dissipation measurements in low stress cyclic loading of metallic materials: from internal friction to micro-plasticity, Mech. Mater. 41 (2009) 928–942, https://doi.org/10.1016/j.mechmat.2009.03.003.
[32] M. Mehdizadeh, M.M. Khonsari, On the role of internal friction in low-and high-cycle fatigue, Int. J. Fatig. 114 (2018) 159–166, https://doi.org/10.1016/j.ijfatigue.2018.05.007.
[33] C.G. Panait, A. Zielińska-Lipiec, T. Koziel, A. Czyrska-Filemonowicz, A. F. Gourgues-Lorenzon, W. Bendick, Evolution of dislocation density, size of subgrains and MX-type precipitates in a P91 steel during creep and during thermal ageing at 600C for more than 100,000h, Mater. Sci. Eng., A 527 (2010) 4062–4069, https://doi.org/10.1016/j.msea.2010.03.010.
[34] W. Ramberg, W.R. Osgood, Description of stress-strain curves by three parameters. https://ntrs.nasa.gov/citations/19930081614, 1943. (Accessed 23 July 2026).
[35] Z. Lopez, A. Fatemi, A method of predicting cyclic stress–strain curve from tensile properties for steels, Mater. Sci. Eng., A 556 (2012) 540–550, https://doi.org/10.1016/j.msea.2012.07.024.
[36] M. Godec, D.A. Skobir Balantič, Coarsening behaviour of M23C6 carbides in creep-resistant steel exposed to high temperatures, Sci. Rep. 6 (2016) 29734, https://doi.org/10.1038/srep29734.
[37] Y. Yang, Y. Chen, K. Sridharan, T.R. Allen, Evolution of carbide precipitates in 2.25Cr-1Mo steel during long-term service in a power plant, Metall. Mater. Trans. A 41 (2010) 1441–1447, https://doi.org/10.1007/s11661-010-0194-6.
[38] Z. Ławrynowicz, Bainitic reaction and microstructure evolution in two normalized and tempered steels designed for service at elevated temperatures, Adv. Mater. Sci. 17 (2017) 22–36, https://doi.org/10.1515/adms-2017-0019.
[39] C. Ji, J. Yao, M. Zhu, Effect of ostwald ripening of carbide particles on mechanical properties of SCM435 steel during subcritical annealing, J. Iron Steel Res. Int. 25 (2018) 724–731, https://doi.org/10.1007/s42243-018-0105-4.
[40] K. Wieczerzak, P. Bala, R. Dziurka, T. Tokarski, G. Cios, T. Koziel, L. Gondek, The effect of temperature on the evolution of eutectic carbides and M 7 C 3 → M 23 C 6 carbides reaction in the rapidly solidified Fe-Cr-C alloy, J. Alloys Compd. 698 (2017) 673–684, https://doi.org/10.1016/j.jallcom.2016.12.252.
[41] D.S. Tsai, T.S. Chin, S.E. Hsu, M.P. Hung, A simple method for the determination of lattice parameters from powder X-ray diffraction data, Mater. Trans. JIM 30 (1989) 474–479, https://doi.org/10.2320/matertrans1989.30.474.

[42] S. Lin, A. Borgenstam, A. Stark, P. Hedström, Effect of Si on bainitic transformation kinetics in steels explained by carbon partitioning, carbide formation, dislocation densities, and thermodynamic conditions, Mater. Charact. 185 (2022) 111774, https://doi.org/10.1016/j.matchar.2022.111774.

[43] M.X. Zhang, P.M. Kelly, Determination of carbon content in bainitic ferrite and carbon distribution in austenite by using CBKLDP, Mater. Charact. 40 (1998) 159–168, https://doi.org/10.1016/S1044-5803(98)00005-9.

[44] C. Garcia-Mateo, J.A. Jimenez, H.W. Yen, M.K. Miller, L. Morales-Rivas, M. Kuntz, S.P. Ringer, J.R. Yang, F.G. Caballero, Low temperature bainitic ferrite: evidence of carbon super-saturation and tetragonality, Acta Mater. 91 (2015) 162–173, https://doi.org/10.1016/j.actamat.2015.03.018.

[45] D. Oleszak, A. Olszyna, Crystallite size and lattice strain determination of NiAl-Al2O3 nanocomposite from X-ray diffraction line broadening, Composites 4 (2004) 284–288.

[46] M. Kopec, D. Przygucka, I. Mierzejewska, R. Sitek, Z.L. Kowalewski, S. Jóźwiak, Effect of printing orientation on microstructure and fatigue behaviour of additively manufactured Haynes 282, J. Alloys Compd. 1036 (2025) 181777, https://doi.org/10.1016/j.jallcom.2025.181777.

[47] L.N. Capaldi, J. Ford, S. Fulco, R.K. Rai, W. Yang, S. Ching, E.A. Stach, K.T. Turner, W. Chen, O.A. Tertuliano, Multiscale fatigue crack initiation in hierarchical additively manufactured alloys, Proc. Natl. Acad. Sci. 123 (2026) e2522790123, https://doi.org/10.1073/pnas.2522790123.

[48] Z. Wang, J. An, M. Xu, H. Zhang, G. Wei, C. Yang, Z. Wei, W. Shen, W. Ding, The mechanism of microstructure refinement and the synergistic strength–ductility enhancement in al–zn–mg–cu alloys processed by continuous rheo-extrusion, Metals 15 (2025) 1167, https://doi.org/10.3390/met15111167.

[49] B. Pyttel, D. Schwerdt, C. Berger, Very high cycle fatigue – is there a fatigue limit? Int. J. Fatig. 33 (2011) 49–58, https://doi.org/10.1016/j.ijfatigue.2010.05.009.

[50] T. Sakai, Review and prospects for current studies on very high cycle fatigue of metallic materials for machine structural use, J. Solid Mech. Mater. Eng. 3 (2009) 425–439, https://doi.org/10.1299/jmmp.3.425.

[51] H. Ming-Yuan, J.W. Hutchinson, Crack deflection at an interface between dissimilar elastic materials, Int. J. Solid Struct. 25 (1989) 1053–1067, https://doi.org/10.1016/0020-7683(89)90021-8.

[52] R. Cappello, G. Meneghetti, M. Ricotta, G. Pitarresi, On the correlation of temperature harmonic content with energy dissipation in C45 steel samples under fatigue loading, Mech. Mater. 168 (2022) 104271, https://doi.org/10.1016/j.mechmat.2022.104271.

[53] R. Jiang, D.J. Bull, A. Evangelou, A. Harte, F. Pierron, I. Sinclair, M. Preuss, X. T. Hu, P.A.S. Reed, Strain accumulation and fatigue crack initiation at pores and carbides in a SX superalloy at room temperature, Int. J. Fatig. 114 (2018) 22–33, https://doi.org/10.1016/j.ijfatigue.2018.05.003.

[54] H. Kleykamp, Thermodynamic studies on chromium carbides by the electromotive force (emf) method, J. Alloys Compd. 321 (2001) 138–145, https://doi.org/10.1016/S0925-8388(01)01012-X.

[55] B. Hallstedt, D. Djurovic, J. Von Appen, R. Dronskowski, A. Dick, F. Körmann, T. Hickel, J. Neugebauer, Thermodynamic properties of cementite, Calphad 34 (2010) 129–133, https://doi.org/10.1016/j.calphad.2010.01.004.

[56] A. Morris, B. Cacciapuoti, W. Sun, The role of small specimen creep testing within a life assessment framework for high temperature power plant, Int. Mater. Rev. 63 (2018) 102–137, https://doi.org/10.1080/09506608.2017.1332538.

[57] G. Webster, R.A. Ainsworth, High Temperature Component Life Assessment, Springer Science & Business Media, 1994.

[58] W. Choi, J. Han, Health-monitoring methodology for high-temperature steam pipes of power plants using real-time displacement data, Appl. Sci. 11 (2021) 2256, https://doi.org/10.3390/app11052256.